

Czech Technical University in Prague
Faculty of Nuclear Sciences and Physical Engineering

Department of Physics
Study programme: Nuclear and Particle Physics



Consequences of new energy calibration of
the KASCADE experiment on the physics
analyses of detected cosmic-ray showers

DIPLOMA THESIS

Author: Bc. Karolína Syrokvaš
Supervisor: Ing. Jakub Vícha, Ph.D.
Year: 2024

České vysoké učení technické v Praze
Fakulta jaderná a fyzikálně inženýrská

Katedra fyziky
Studijní program: Jaderná a částicová fyzika



Vliv nové energetické kalibrace experimentu
KASCADE na fyzikální analýzy
detekovaných spršek kosmického záření

DIPLOMOVÁ PRÁCE

Vypracovala: Bc. Karolína Syrokvaš
Vedoucí práce: Ing. Jakub Vícha, Ph.D.
Rok: 2024

ZADÁNÍ DIPLOMOVÉ PRÁCE

Akademický rok: 2022/2023



Student: Bc. Karolína Syrokvaš

Studijní program: Jaderná a částicová fyzika

Název práce: Vliv nové energetické kalibrace experimentu KASCADE na fyzikální
(česky) analýzy detekovaných spršek kosmického záření

Název práce: Consequences of new energy calibration of the KASCADE experiment
(anglicky) on the physics analyses of detected cosmic-ray showers

Jazyk práce: Angličtina

Pokyny pro vypracování:

- 1) Stanovení nové energetické kalibrace experimentu KASCADE pomocí nových modelů hadronických interakcí.
- 2) Určení frakce neviditelné energie spršek v optických měřeních jako funkce kalorimetrické energie.
- 3) Odhadnutí vlivu nové kalibrace na energetické spektrum lehkých a těžkých částic kosmického záření.
- 4) Odhadnutí vlivu této kalibrace na množství sekundárních mionů detekovaných na zemi.

Doporučená literatura:

- [1] T. Antoni et al., The cosmic-ray experiment KASCADE, NIM A 513 (2003) 490.
[2] A. Haungs et al., The KASCADE Cosmic-ray Data Centre KCDC: granting open access to astroparticle physics research data, EPJ C 78 (2018) 741.
[3] W. D. Apel et al., KASCADE-Grande measurements of energy spectra for elemental groups of cosmic rays, Astropart. Phys. 47 (2013) 54.
[4] J. C. A. Velazquez et al., Estimations of the muon content of cosmic ray air showers between 10 PeV and 1 EeV from KASCADE-Grande data, PoS(ICRC2021)376, doi.org/10.22323/1.395.0376.

Jméno a pracoviště vedoucího diplomové práce:

Ing. Jakub Vícha, Ph.D.
Fyzikální ústav AV ČR, v.v.i.

Konzultant:

RNDr. Vladimír Novotný, Ph.D.
Fyzikální ústav AV ČR, v.v.i.

Mgr. Michal Broz, Ph.D.

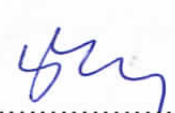
Katedra fyziky, Fakulta jaderná a fyzikálně inženýrská ČVUT v Praze

Datum zadání diplomové práce: 20.10.2022

Termín odevzdání diplomové práce: 03.05.2023

Doba platnosti zadání je dva roky od data zadání.


.....
garant studijního programu


.....
vedoucí katedry




.....
děkan

V Praze dne 20.10.2022



PROHLÁŠENÍ

Já, níže podepsaný(á)

Jméno a příjmení studenta: Karolína Syrovkaš
Osobní číslo: 473938
Studijní program: Jaderná a částicová fyzika
Studijní obor: /
Specializace: /

prohlašuji, že jsem diplomovou práci s názvem:

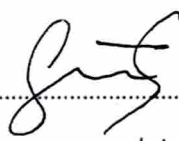
Vliv nové energetické kalibrace experimentu KASCADE na fyzikální analýzy detekovaných spršek kosmického záření

vypracoval(a) samostatně a uvedl(a) veškeré použité informační zdroje v souladu s Metodickým pokynem o dodržování etických principů při přípravě vysokoškolských závěrečných prací.

Rovněž souhlasím s porovnáním textu mé kvalifikační práce s databází kvalifikačních prací Theses.cz provozovanou Národním registrem vysokoškolských kvalifikačních prací a systémem na odhalování plagiátů.

V Praze dne

6.1.2024


.....
podpis

Acknowledgements

I would like to thank my supervisor, Ing. Jakub Vícha, Ph.D., for the introduction to the experiment KASCADE, and the subject-matter of energy reconstruction. I would also like to thank the whole astroparticle group, namely Mgr. Vladimír Novotný, Ph.D. and Mgr. Jan Ebr, Ph.D. for providing additional simulations needed for this analysis. Last but not least, I would like to thank my family, and my boyfriend Ing. Nikolas Denner for his emotional and technical support.

Bc. Karolína Syrokvaš

Název práce:

Vliv nové energetické kalibrace experimentu KASCADE na fyzikální analýzy detekovaných spršek kosmického záření

Autor: Bc. Karolína Syrokvaš

Studijní program: Jaderná a částicová fyzika

Obor: /

Druh práce: Diplomová práce

Vedoucí práce: Ing. Jakub Vícha, Ph.D.

Oddělení astročásticové fyziky, Fyzikální Ústav Akademie věd České republiky, v. v. i.

Konzultant: RNDr. Vladimír Novotný, Ph.D.

Oddělení astročásticové fyziky, Fyzikální Ústav Akademie věd České republiky, v. v. i.

Abstrakt: Experiment KASCADE byl povrchový detektor zaznamenávající hustotu sekundárních částic rozsáhlých atmosférických spršek vzniklých interakcí primárního kosmického záření s atmosférickými jádry. V této práci navrhujeme nový způsob rekonstruování energie spršek kosmického záření detekovaných experimentem KASCADE. Použijeme přitom dodatečnou informaci o velikosti sklonu laterální distribuční funkce signálu s jako dalšího parametru. Využíváme spojení univerzálního vztahu mezi tzv. chybějící energií spršky při optické detekci a počtem mionů detekovaných na zemi, dále vztahu mezi kalorimetrickou energií spršky a počtem nabitých částic na zemi. Tento nový způsob určení energie spršky, jako součet kalorimetrické a chybějící energie, poskytuje lepší odhad energie spršky než standardním způsobem. Odhadujeme vliv této nové energetické kalibrace na energetickou závislost počtu mionů, frakce neviditelné energie, a energetická spektra lehkých, středně těžkých a těžkých částic společně s celkovým energetickým spektrem.

Klíčová slova: Spršky kosmického záření, rekonstrukce energie, chybějící energie, miony v atmosférických sprškách, energetické spektrum kosmického záření, experiment KASCADE.

Title:

Consequences of new energy calibration of the KASCADE experiment on the physics analyses of detected cosmic-ray showers

Author: Bc. Karolína Syrokvaš

Abstract: The experiment KASCADE was a surface detector observing the secondary particles of the extensive air showers produced by the interaction of primary cosmic rays with the atmospheric nuclei. We propose a new energy reconstruction formula of the experiment KASCADE by utilising the shape parameter s of the reconstructed lateral distribution function. We apply a universal relation between the invisible energy during optical detection and the number of muons measured at ground by the KASCADE experiment, along with the relation between the calorimetric energy and the number of charged particles measured at ground. This new energy estimator, as a sum of invisible and calorimetric energy, provides an improved estimation of the shower energy than the standard energy estimator. We estimate the consequences of this new energy calibration, such as the change in the energy dependence of the muon number, the invisible energy fraction, and the energy spectrum of light, medium-heavy and heavy particles along with the total energy spectrum.

Key words: Cosmic ray air showers, energy reconstruction, invisible energy, muons in air showers, energy spectrum of cosmic rays, the KASCADE experiment.

Contents

Introduction	11
1 Cosmic-ray showers	13
1.1 Primary particles	13
1.1.1 Mass distribution	13
1.1.2 Energy spectrum	14
1.2 Extensive air showers	17
1.2.1 Heitler - Matthews model	17
2 Simulations of extensive air showers	23
2.1 Simulation program CORSIKA	23
2.2 Simulation program CONEX	24
2.3 Hadronic interaction models	25
2.3.1 Sibyll 2.3	25
2.3.2 QGSJet-II 04	25
2.3.3 EPOS LHC	26
3 The KASCADE experiment	27
4 KASCADE data and simulations	31
4.1 The KASCADE Cosmic ray Data Centre KCDC	31
4.2 Current energy estimation formula	31
4.3 Data selection	32
4.3.1 Additional simulations	32
4.3.2 KASCADE simulations	33
4.3.3 KASCADE data	33
5 New energy estimation from KASCADE data	35
5.1 Invisible energy	36
5.2 Calorimetric energy	38
5.3 Comparison of energy estimation formulae	40
6 Consequences of new energy calibration	45
6.1 Energy dependence of muon number	45
6.2 Invisible energy fraction	47
6.3 Mass-dependent energy spectrum	48
6.3.1 Light and heavy particles	48
6.3.2 Light, medium-heavy and heavy particles	50

Conclusions	53
Bibliography	55
Appendix	59
A Energy reconstruction	59
A.1 Values of the new energy reconstruction	59
A.2 Biases and resolutions of other models	60
A.2.1 Biases with respect to true energy	60
A.2.2 Resolutions with respect to true energy	61
A.2.3 Biases with respect to reconstructed energy	62

Introduction

The ionisation of the atmosphere was first discovered in the 19th century [1] and the search for its cause led to the discovery of cosmic rays. Due to its penetrating power, the nature of cosmic rays was generally believed to be purely γ radiation. It was later found that cosmic rays interact with the Earth's geomagnetic field and were, therefore, mostly comprised of charged particles. The interaction with the geomagnetic field further showed that cosmic rays are primarily positively charged, and thus mostly protons.

Today, we know that cosmic rays are extraterrestrial particles reaching energies larger than those achievable by modern colliders. Until the 1940s, they were the only source of high energy particles. With the development of cosmic-ray physics, particle physics began to emerge, and many fundamental discoveries were made thanks to the study of cosmic rays. By 1955, however, significant progress in collider technology allowed for particle physics experiments to be largely dominated by accelerators. Still, within the conditions on Earth it is currently impossible to reach energies as large as those found in high-energy cosmic rays.

With the study of cosmic rays the main questions that arise are its energy spectrum, mass distribution and which sources are capable of accelerating matter to the highest energies [2]. The changes in mass distribution and sources of cosmic rays are most prominent close to the structures observed in the energy spectrum of cosmic rays: the knee (energy $\sim 3.5 \cdot 10^{15}$ eV), the second, or iron, knee (energy $\sim 10^{17}$ eV [3]), the ankle (energy $\sim 5 \cdot 10^{18}$ eV), the instep (energy $\sim 13 \cdot 10^{18}$ eV [4]), and the toe (energy $\sim 46 \cdot 10^{18}$ eV [4]), with the highest energy recorded being the so-called Oh-My-God particle $\sim 3.2 \cdot 10^{20}$ eV [5].

Cosmic rays above $\sim 10^{15}$ eV are rare and can only be observed on Earth by detecting the resulting extensive air shower produced by the collision of the primary cosmic rays with a nucleus of the atmosphere. Due to our lack of knowledge about hadronic interactions taking place during nucleus-nucleus collisions, the reconstruction of the observables of the original cosmic particle is burdened with large systematic uncertainties.

In this work, we strive to address these uncertainties by analysing data produced by the cosmic-ray experiment KASCADE [6]. The first chapter briefly introduces the reader to cosmic rays, including the difference between the primary and secondary cosmic rays. The known mass spectrum and energy spectrum is described, and the development of extensive air showers, divided into electromagnetic showers, hadronic showers and the multi-nuclei showers follow. The reader is also introduced to the

hadronic interaction models and simulation programs used in this work, along with their differences.

In the second chapter, the cosmic-ray experiment KASCADE is introduced. The history and layout of the experiment is described, along with its detection mechanisms and observable energy range. The KASCADE Cosmic ray Data Centre KCDC [7] is also introduced in the third chapter, along with the aim of the project and the description of its use. We further introduce the old energy estimation formula used by the KASCADE experiment and the data selected for this analysis in the fourth chapter.

In the fifth chapter, the new energy estimation is described along with the steps taken to produce the estimation formula. The comparison of energy biases of the old estimation formula and the new formula is shown. The sixth chapter shows the consequences of the new energy calibration, such as the energy dependence of the muon number, the invisible energy fraction, and the spectrum of light and heavy particles, along with the energy spectrum of light, heavy and moderate particles.

Chapter 1

Cosmic-ray showers

Cosmic rays consist of high-energy charged particles of extraterrestrial origin. These are called primary particles, which, while traversing the atmosphere, generate a shower of secondary particles. This chapter describes the mass distribution and energy spectrum of primary cosmic rays, as well as the development of the cosmic ray air showers.

1.1 Primary particles

1.1.1 Mass distribution

The charged primary particles consist mostly of protons (86%), alpha particles (11%), heavier nuclei up to iron (1%) and electrons (2%) [8]. There are also small portions of even heavier nucleons, antiprotons and positrons, generated possibly via interactions with interstellar gas. Neutral primary particles consist of γ -rays, neutrons and neutrinos. Due to the absence of charge, and consequently no bending in magnetic fields, it is possible to identify the source from which these particles are coming, such as solar neutrinos.

The majority of arriving cosmic rays is of galactic origin. For energies above 8 EeV, the cosmic rays are dominated by particles of extra-galactic origin, as the galactic magnetic field is not capable of containing particles with energies above 10^{20} eV inside the galaxy during the acceleration processes. No astrophysical sources capable of such acceleration are known.

The chemical composition of many of the cosmic-ray nuclei is similar to the solar system abundances deduced from absorption lines in the photosphere of the Sun and meteorites, shown in Figure 1.1. Both compositions show the odd-even effect, meaning nuclei with even number of protons and neutrons are more strongly bound than nuclei with odd number of either protons, neutrons, or both, making odd-odd nuclei more stable products in stellar thermonuclear reactions. The normalised peaks in abundances for carbon (C), nitrogen (N), oxygen (O) and iron (Fe) are also very alike, implying stellar origin of many cosmic-ray nuclei at the lowest energies.

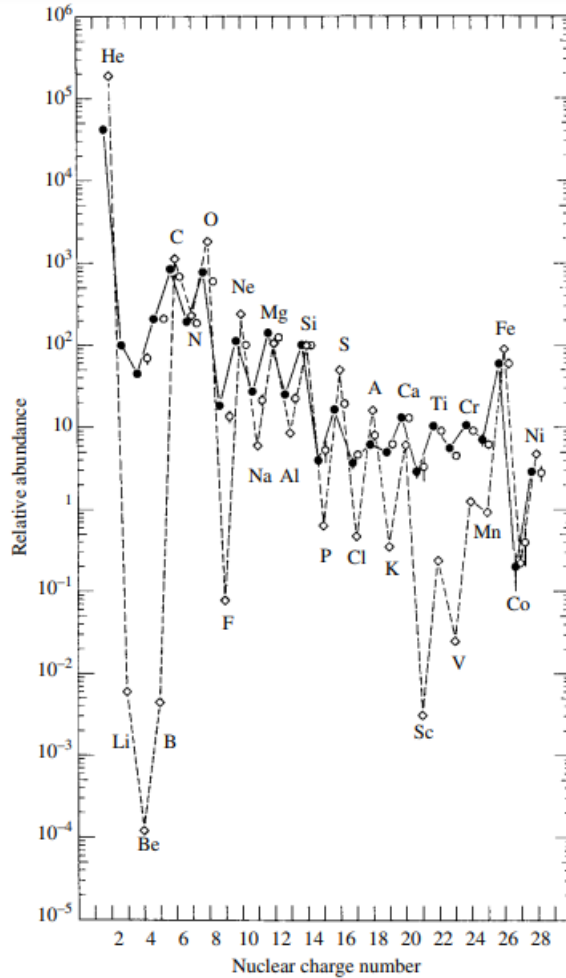


Figure 1.1: The chemical composition of primary cosmic-ray nuclei, shown as a full-line, compared with the solar abundances, shown as a dashed line. From [8].

The major differences are seen in lithium (Li), beryllium (Be) and boron (B), as such elements are not common in stars due to their low Coulomb barriers and are weakly bound. These elements are rapidly consumed in stellar cores during nuclear reactions. This difference is caused by spallation of primary carbon and oxygen nuclei. Moreover, the energy spectra of lithium, beryllium and boron are steeper than those of carbon or oxygen [8]. The abundance of scandium (Sc), titanium (Ti), vanadium (V) and manganese (Mn) can be similarly explained by the spallation of the iron and nickel (Ni) nuclei.

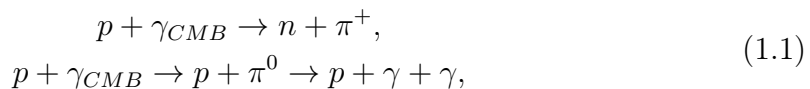
1.1.2 Energy spectrum

A wide range of energies is observed in cosmic rays, exceeding energies of 10^{20} eV, and can be represented by a power-law distribution [9], as seen in Figure 1.2. The energy spectrum shows important structures mentioned in the introduction; it is convenient to distinguish cosmic rays using these structures.

The origin of the knee is thought to be caused by light particles such as protons

or alpha particles with energy large enough to escape the magnetic field of galactic sources. The energy region between the knee and the ankle is generally considered as the transition between particles that cannot escape the magnetic fields of galactic sources and the particles of extragalactic origin. All particles beyond the ankle are usually considered to be of extragalactic origin. The steep end of the energy spectrum may be related to the GZK cut-off, the upper energy limit of cosmic accelerators.

The GZK¹ cut-off is the theoretical upper limit of the energy of cosmic rays. It is caused by the interaction of high energy cosmic rays with the cosmic microwave background (CMB). Cosmic ray protons with the highest energies have Lorentz factors $\gamma = \frac{1}{\sqrt{1-\beta^2}}$, $\beta = \frac{v}{c}$, where v is the particle velocity, great enough for the CMB photons to have great energies in their rest frame. During the interaction, mainly the following reactions take place



producing particles with smaller energies than the original proton, losing approximately 20% of its energy.

The shape of the low-energy spectrum (energies $< 10^9$ eV) is affected by the phase of the solar cycle. The flux of the low-energy galactic cosmic rays is suppressed during greater solar activity, whereas during low solar activity, the flux is at maximum. This phenomenon caused by the cosmic rays diffusing through the solar wind and influencing the repulsion power of the geomagnetic field is known as solar modulation of cosmic rays.

Taking solar modulation in the account, the differential energy spectra of various types of cosmic rays can be represented by the power-law distribution of the flux of particles $N(E)$ on the energy of the primary particle E

$$N(E)dE = K \cdot E^{-x}dE, \tag{1.2}$$

where K is a normalisation constant and x is a parameter of the steepness of the spectrum, equal roughly to 2.7.

The evolution of the fluxes of various primaries can be seen in Figure 1.3, in which the global spline fit (GSF) model is used.

¹Named after Kenneth Greisen, Georgiy Zatsepin and Vladimir Kuzmin, who calculated the value of this energy in 1966 [10] [11].

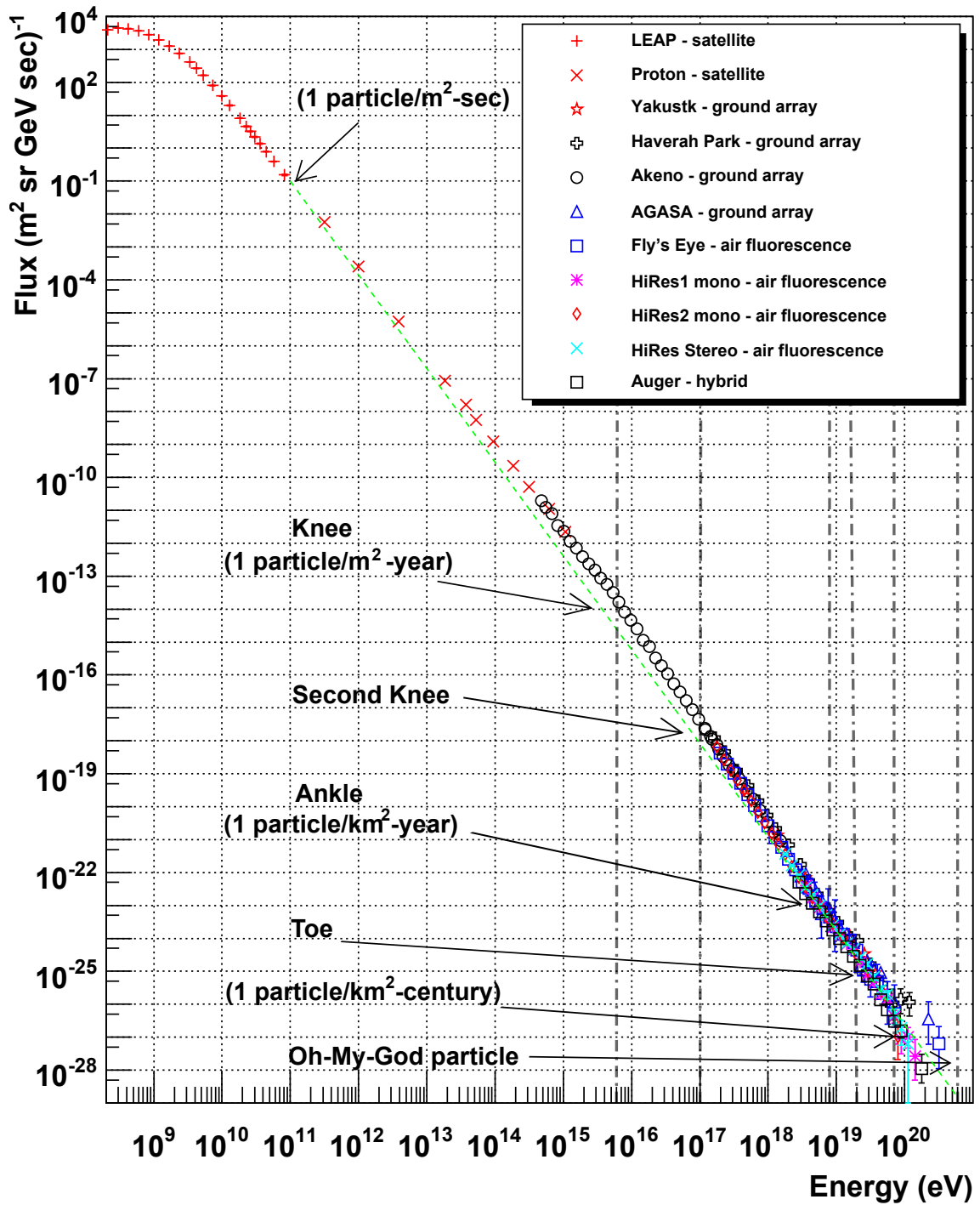


Figure 1.2: Power-law distribution of the cosmic-ray energy spectrum along with the cosmic ray spectra from various experiments. Arrows point at significant energies with their respective frequencies of arrival of particles, green dashed line represents a power-law, see equation (1.2), for $x = 2, 7$. From <https://www.physics.utah.edu/~whanlon/spectrum.html>, modified.

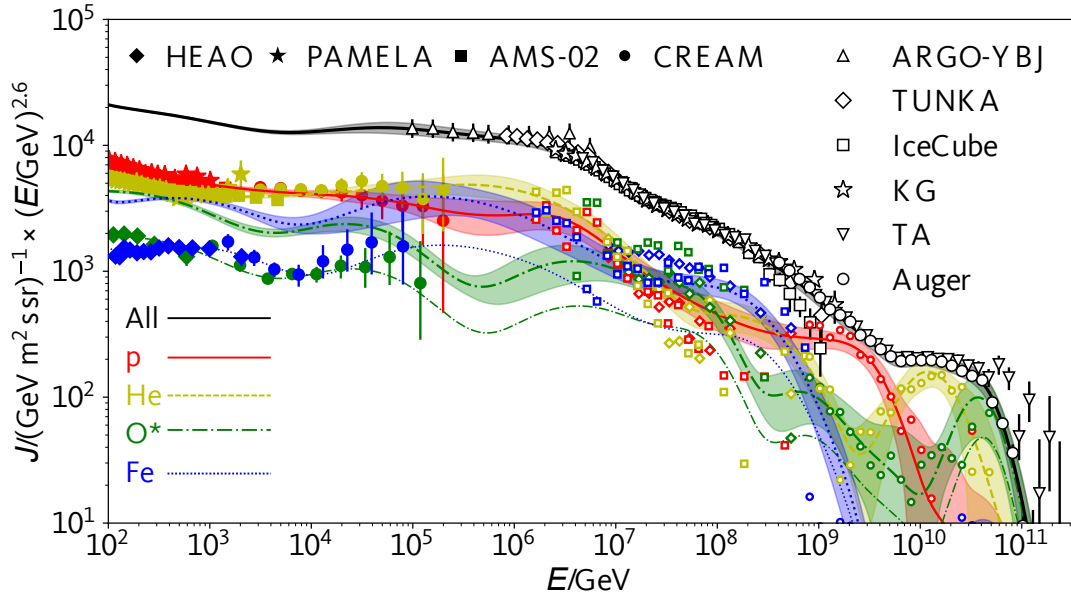


Figure 1.3: The all-particle flux (black solid line), the flux contributed by protons (red solid line), helium (yellow dashed line), the oxygen group (green dash-dotted line) and the iron group (blue dotted line). Bands around the model line show a variation of one standard deviation. Data points show measurements which were energy-scale adjusted. Error bars represent combined statistical and systematic uncertainties. Data points of composition measurements from air-showers are not shown without error bars for clarity. In case of oxygen and iron, both the elemental flux and the group flux are shown; the smaller flux without error band is the elemental flux in each case. TA stands for Telescope Array, KG for KASCADE-Grande. From [12].

1.2 Extensive air showers

Many experimental methods have been created to characterise the features of an air shower [2]. It is necessary to estimate both mass and energy of the primary particle independently, usually by observing either the longitudinal development of the extensive air shower (EAS) or by determining the electromagnetic and muonic components at ground level. The theoretical understanding of the shower development and the hadronic interactions occurring within the cascade shapes the ability to deduce the composition of cosmic rays on a statistical basis.

1.2.1 Heitler - Matthews model

Electromagnetic shower

Extensive air showers develop as a complex combination of hadronic cascades and hadronic multiparticle production, during which up to 10^{10} charged high energy particles are generated [14]. Before high-speed computing, Heitler presented a simple

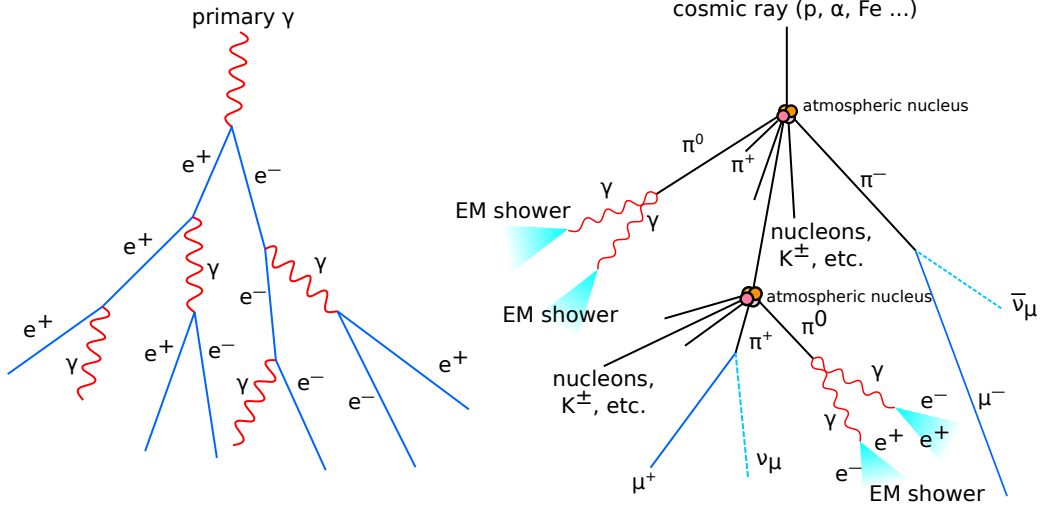


Figure 1.4: *Left:* Electromagnetic air shower generated by a primary γ ray and purely composed of electron-positron pairs and photons. *Right:* Hadronic cascade originated by a hadronic particle (proton or nucleus) producing a large variety of secondary particles. From [13], modified.

model of electromagnetic cascade development [15], where electrons e^- , positrons e^+ and photons γ undergo repeated two-body splittings, either bremsstrahlung or e^-e^+ pair production, see left panel of Figure 1.4. Each particle from an electromagnetic shower undergoes such splitting after travelling one splitting length

$$d = \lambda_r \ln 2, \quad (1.3)$$

where λ_r is the radiation length of the medium. It is assumed that the energy of the particle is equally divided between the two outgoing particles. After n splittings, traversing the distance of $x = n\lambda_r \ln 2$, the total number of particles in the shower is $N = 2^n = e^{\frac{x}{\lambda_r}}$. This number is also known as the shower size. The multiplication process ceases once the energies of the particles are too low for pair production or bremsstrahlung to occur, and the collision energy loss becomes greater than the radiative energy loss. Heitler named this energy the critical energy ξ_c^e . If we consider a shower initiated by a photon with energy E_0 , then the number of particles produced by this cascade is $N = N_{\max}$, where each particle has the energy $\xi_c^e = \frac{E_0}{N_{\max}}$. The penetration depth X_{\max} at which the shower reaches the maximum size is determined by the number of splitting lengths n_c required for the energy per particle to be reduced to the critical energy. Since $N_{\max} = 2^{n_c}$, then

$$n_c = \frac{\ln\left(\frac{E_0}{\xi_c^e}\right)}{\ln 2}, \quad (1.4)$$

and we get the equation for the depth of shower maximum for electromagnetic cascades

$$X_{\max}^{\gamma} = n_c \lambda_r \ln 2 = \lambda_r \ln \left(\frac{E_0}{\xi_c^e} \right), \quad (1.5)$$

from which can be seen that X_{\max}^{γ} grows logarithmically with the energy of the primary particle.

Hadronic showers

A hadronic shower is essentially a pion production process, see right panel of Figure 1.4. The main difference between a hadronic shower and a pure electromagnetic shower is the loss of a third of the energy during each particle production caused by the near-instant decay of neutral pions π^0 to two photons. The energy of the initial primary particle is divided between two channels, electromagnetic and hadronic, and is approximately linearly proportional to the number of electromagnetic particles and the number of muons μ^{\pm} generated from the decay of charged pions π^{\pm} .

Air showers initiated by hadrons are treated similarly to the Heitler's electromagnetic showers [14]. The atmosphere is divided into layers with fixed thickness $\lambda_I \ln 2$, where λ_I is the interaction length of strongly interacting particles, assumed constant for energies in the range 10 - 1000 GeV. After traversing one layer, N_{ch} charged pions and $\frac{1}{2}N_{\text{ch}}$ neutral pions are produced. The neutral pions decay immediately to photons, initialising an electromagnetic shower, while the charged pions continue through another layer and interact. This process repeats until the energy of the charged pions falls below the critical energy ξ_c^{π} , below which they rather decay into muons. We assume that ξ_c^{π} is the energy where the interaction length of pions is equal to the decay length.

If we consider a single cosmic-ray proton entering the atmosphere with energy E_0 , then after n interactions, or atmosphere layers, $N_{\pi} = (N_{\text{ch}})^n$ charged pions are produced. After n interactions, one pion carries the energy

$$E_{\pi} = \frac{E_0}{\left(\frac{3}{2}N_{\text{ch}}\right)^n}, \quad (1.6)$$

and after n_c interactions, this energy falls below the critical energy ξ_c^{π} .

The primary energy is divided between N_{π} pions, which decay into $N_{\mu} = N_{\pi}$ muons, and N_{\max} electromagnetic particles in subshowers. The total energy is then

$$E_0 = \xi_c^e N_{\max} + \xi_c^{\pi} N_{\mu}. \quad (1.7)$$

The number of electrons is scaled as $N_e = \frac{N_{\max}}{g}$, where $g = 10$ is the correction factor, considered an order of magnitude estimate, and we assume that the values of the critical energies are constant: $\xi_c^e = 85$ MeV, $\xi_c^{\pi} = 20$ GeV, $\lambda_I = 120$ g·cm⁻², $\lambda_r = 37$ g·cm⁻². Then we get an equation representing the energy conservation:

$$E_0 = g\xi_c^e \left(N_e + \frac{\xi_c^\pi}{g\xi_c^e} N_\mu \right) \approx (N_e + 24 \cdot N_\mu) \cdot 0.85 \text{ GeV}. \quad (1.8)$$

The depth of shower maximum $X_{\text{max}}^{\text{P}}$ is the atmospheric depth at which the electrons and photons reach their maximum size. The first estimation of the dependence of $X_{\text{max}}^{\text{P}}$ on E_0 uses only the electromagnetic cascade generated from the first decay of π^0 , carrying energy $\frac{1}{3}E_0$. To properly evaluate $X_{\text{max}}^{\text{P}}$, summing each generation of electromagnetic subshowers is necessary. However, this is beyond the simple model used.

The first interaction occurs at depth $X_0 = \lambda_{\text{I}} \ln 2$, where λ_{I} is the interaction length of the primary proton. During this interaction $\frac{1}{2}N_{\text{ch}}$ neutral pions are generated, decaying immediately to N_{ch} photons. Each of these photons trigger parallel electromagnetic cascades with the energy $\frac{E_0}{3N_{\text{ch}}}$. These showers reach their maximum at

$$X_{\text{max}}^{\text{P}} = X_0 + \lambda_{\text{r}} \ln \left(\frac{E_0}{3N_{\text{ch}}\xi_c^e} \right), \quad (1.9)$$

which, after inserting previously mentioned values, is lower than a value predicted by detailed simulations by about $100 \text{ g}\cdot\text{cm}^{-2}$, or about $2\lambda_{\text{I}}$ [14]. This is expected, as generations after the first electromagnetic cascade were neglected. It is appropriate to compare an air shower produced by a primary proton to pure electromagnetic cascade:

$$X_{\text{max}}^{\text{P}} = X_{\text{max}}^{\gamma} + X_0 - \lambda_{\text{r}} \ln (3N_{\text{ch}}). \quad (1.10)$$

According to this treatment, photon-induced showers penetrate the atmosphere deeper than the proton-induced showers. The muon size of the shower is

$$\ln N_\mu = \ln N_\pi = \beta \ln \left(\frac{E_0}{\xi_c^\pi} \right), \quad (1.11)$$

where

$$\beta = \frac{\ln N_{\text{ch}}}{\ln \frac{2}{3}N_{\text{ch}}} = 0.85. \quad (1.12)$$

Superposition model

If the primary particle is a nucleus with atomic number A and total energy E_0 , we treat the produced shower as A individual showers initialised by a free nucleon, evolving independently on each other and carrying energy $\frac{E_0}{A}$. Since strong interaction does not differentiate neutron and protons, we treat the nucleus-induced shower as A independent proton showers at the same point. The number of produced muons is then

$$N_{\mu}^A = N_{\mu}^P \cdot A^{0.15}, \quad (1.13)$$

where N_{μ}^P is the number of muons produced by a single proton shower. For the depth of shower maximum and initial energy we then have

$$X_{\max}^A = X_{\max}^P - \lambda_r \ln A, \quad (1.14)$$

$$E_0 = (N_e + 25 \cdot N_{\mu}) \cdot 0.85 \text{ GeV}. \quad (1.15)$$

Showers initialised by heavier nuclei produce more muons, caused by the less-than-linear growth of the muon number with energy. Nucleons with lower energy generate fewer interaction generations, losing less energy to electromagnetic components. Iron showers will have $56^{0.15} \times = 1.8 \times$ more muons at the shower maximum than proton showers of the same energy. Showers initiated by heavier nuclei reach their maximum shower depth higher in the atmosphere. An iron shower will have its maximum $\lambda_r \ln 56 \text{ g}\cdot\text{cm}^{-2} = 150 \text{ g}\cdot\text{cm}^{-2}$ higher than a proton shower of the same energy according to this model.

Chapter 2

Simulations of extensive air showers

The Monte Carlo method is most commonly used to simulate extensive air showers [16]. However pure Monte Carlo simulations are impractical for showers initiated by a primary particle with extremely high energy due to large computing time requirements. This could be solved by implementing the so-called "thinning" method, or "thin sampling", during which only a small number of particles is simulated explicitly, assigning a weight factor. A shower initiated by a primary with energy above 10^{20} eV would have to be simulated for more than one year even with today's fast computing stations without the implementation of the thin sampling. This approach is used by the simulation program CORSIKA [17].

An alternative approach is used by the simulation program CONEX, a one-dimensional hybrid simulation program. The development of an air shower is described by cascade equations, and only the most energetic part is described using Monte Carlo simulations.

2.1 Simulation program CORSIKA

CORSIKA, short for COsmic Ray SIMulations for KAscade, is a Monte Carlo extensive air-shower simulator originally developed for the experiment KASCADE. This simulator was improved by implementing the Landau-Pomeranchuk-Migdal effect for simulating showers initiated by particles at the highest energies.

As this simulation program is three-dimensional, it requires information about the atmosphere in which the air shower develops and the position of the ground level. The simulated atmosphere contains layers and is simulated as flat, neglecting Earth's curvature.

Before the shower is simulated, the thinning energy E_{thin} , usually represented as a fraction of the primary energy E_0 , is chosen, and the thinning fraction is expressed as

$$\varepsilon_{\text{thin}} = \frac{E_{\text{thin}}}{E_0}. \quad (2.1)$$

Once the secondary particles energies fall below E_{thin} , one secondary particle is randomly chosen while respecting the probability of the particle surviving

$$p_i = \frac{E_i}{\sum_j E_j}, \quad (2.2)$$

where E_i is the energy of the chosen particle, and E_j are the energies of all other secondary particles considered. After the selection, the weight factor of this particle is $w_i = \frac{1}{p_i}$. Secondary particles with lower energies are still calculated, but are treated differently depending on whether their energy is higher or lower than E_{thin} . If their energy sum is higher than E_{thin} , more than one secondary particle is kept for the further Monte Carlo simulation development.

The computing time rises with lower E_{thin} , while with higher E_{thin} the uncertainties of the observable increase due to statistical fluctuations during the thinning process. The optimal thinning energy depends on the specific requirements of the simulations.

2.2 Simulation program CONEX

As mentioned above, CONEX is a one-dimensional hybrid simulation program of extensive air showers [16]. The air shower simulation itself has two phases: an explicit Monte Carlo simulation for particles with energy higher than a chosen threshold energy E_{thr} , and a solution of nuclear-electro-magnetic cascade equations for smaller sub-showers with energy below E_{thr} .

In the hadronic part of the air shower, the propagation, interaction and, if possible, decay of nucleons, antinucleons, charged pions and kaons is tracked. All other types of hadrons are simulated to decay immediately. The interactions in Monte Carlo simulations are governed by the hadronic interaction programs.

The electromagnetic part is simulated with EGS4 code [18], which is another Monte Carlo generator, which includes Landau-Pomeranchuk-Migdal effect for high-energy electrons, positrons and photons [19]. The simulation of photonuclear reactions and muon pair production is the same as in Monte Carlo simulations [17]. Ionisation losses of electrons and positrons are described using Bethe-Bloch formula with density correction [20]. The interactions of high energy muons are only kept in Monte Carlo simulations, and neglected in cascade equations.

In general, one shower is simulated as follows: a primary particle has a given energy, direction describing the real shower axis and the shower trajectory, and a position in the atmosphere, which, unless specified otherwise, is 100 km above sea level. If the primary particle is hadron, a hadronic cascade is simulated, until all produced secondary particles have energy below E_{thr} . All subthreshold hadrons, muons and electromagnetic particles are recorded in tables, from which the initial parameters for cascade equations are created. Above-threshold electromagnetic particles are moved to EGS4 and simulated, and sub-threshold electromagnetic particles are added to the initial parameters for electromagnetic cascade equations.

In the next phase, the appropriate cascade equations with their initial parameters are calculated for the first depth level, obtaining discrete spectra of various hadrons. Sub-threshold electromagnetic cascade equations are calculated. The produced particles are made to be initial parameters for cascade equations for the second depth level. This process is repeated in all following depth levels.

2.3 Hadronic interaction models

The choice of hadronic interaction model affects the cosmic-ray observables, namely the mass-sensitive number of muons at ground and the depth of the shower maximum. To determine the properties of the primary particle, identification of the ways how different models describe the experimental data is crucial. This is the reason behind the use of multiple hadronic interaction models for the description of observed showers. A prediction of accelerator data is required to estimate the systematic uncertainties of extrapolations to higher energies. For the simulation program CORSIKA, these hadronic interaction models are used in the highest energies; at lower energies, the hadronic interaction model FLUKA [21], developed at CERN, is used. An example of different predictions of various hadronic interaction models can be seen in Figure 2.1

2.3.1 Sibyll 2.3

Sibyll is one of the first hadronic interaction models developed specifically for the cosmic-ray data interpretation [22], starting development in 1980s. The version **Sibyll 2.3** was released in 2016 and improved in the versions **Sibyll 2.3c** and **Sibyll 2.3d**. The main ideas of this model is the combination of the simulation of hadron production described non-perturbatively and perturbative quantum chromodynamics computations. While this model is less complicated and sophisticated than other modern models, it still correctly predicts some of the accelerator data, such as those from the LHC. The version Sibyll 2.3d specifically improved mainly the description of the leading particles, which cause an increase of the generated number of muons by 20% - 50%, making it the generator predicting the largest number of muons in comparison with other models [23].

2.3.2 QGSJet-II 04

The model **QGSJet** simulates hadronic interactions based on the Quark-Gluon String (QGS) model [24]. This model uses theoretical extrapolation of accelerator data to higher energies, where hadron collisions are calculated as multiple scattering processes and repeating elemental scatterings are calculated as microscopic parton cascades [25]. These repeating scatterings are considered independently, leading to the neglect of non-linear effects, which is corrected in the **QGSJet-II 04** update.

2.3.3 EPOS LHC

EPOS treats the collision as a quantum-mechanical scattering of multiple particles [26]. Hadron-hadron interactions are interpreted as an exchange of parton ladders between hadrons. EPOS implements effect of high parton density at high energies and small impact parameters and has a different approach to the central part of the collision compared to other models. The improved version **EPOS LHC** was developed for detailed description of the new LHC data [27], since older models had problems describing proton-proton collisions due to the effects observed during heavy collisions. It differs in muon production, predicting more muons than QGSJet-II 04 or Sibyll 2.1, while still predicting less than Sibyll 2.3d.

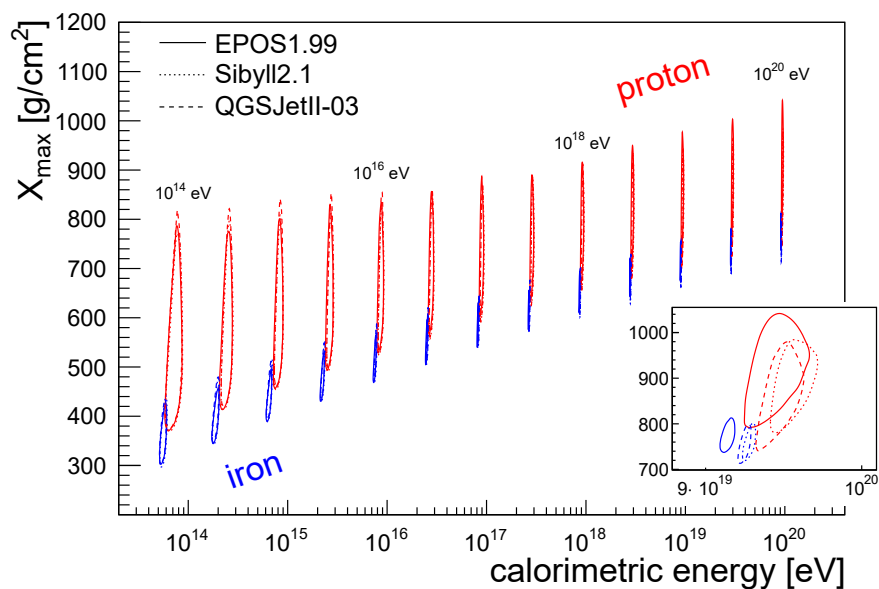


Figure 2.1: Air shower simulation of the shower maximum vs. calorimetric energy. Contour lines illustrate the regions which include 90 % of the showers and the insert shows a detailed view at 10^{20} eV. From [2].

Chapter 3

The KASCADE experiment

KASCADE (KArlsruhe Shower Core and Array Detector) was designed to measure extensive air showers produced by cosmic rays of primary energy above 10^{15} eV [6] and to investigate the structure in the energy spectrum of the cosmic rays known as the knee (energy $\sim 10^{15.5}$ eV). The experiment started data acquisition in 1996 and was further extended to KASCADE-Grande in 2003 to reach higher energies of primary cosmic rays. While the experiment ceased taking data in 2012¹, the international collaboration of the experiment continues the detailed analysis of nearly 20 years of data taken. This data is made publicly available on the web portal of the KASCADE Cosmic ray Data centre [7].

The experiment itself was situated at the laboratory site of Forschungszentrum Karlsruhe in the Rhine valley at 110 m a.s.l. [6]. The muonic and electromagnetic components of air showers were recorded simultaneously and independently. The electromagnetic component was measured with an array of scintillation counters, while the muonic component was measured by shielded scintillators and tracking chambers at four different energy thresholds. The hadronic component was measured using a sampling calorimeter.

The detector array comprised of scintillation detectors housed in 252 stations on a grid organised in clusters of 16 stations, where the inner clusters had only 15 stations. The schematic layout of the experiment can be seen in Figure 3.1. The layout was optimised using air showers generated with CORSIKA that had been tracked through the detection simulation code CRES, simulating the response of the KASCADE detector array. The detector coverage of 1.3% for the electromagnetic and 1.5% for the muonic component was chosen. With this level of sampling the accuracy in air shower reconstruction is dominated by shower fluctuations and not by the sampling statistics. All data are analysed offline using the data reconstruction program KRETA (KASCADE Reconstruction of ExTensive Air showers).

¹The date of the last event recorded by KASCADE-Grande is 15th November 2012, while the KASCADE array and the radio antenna field LOPES recorded their last event on 15th January 2013 [28].

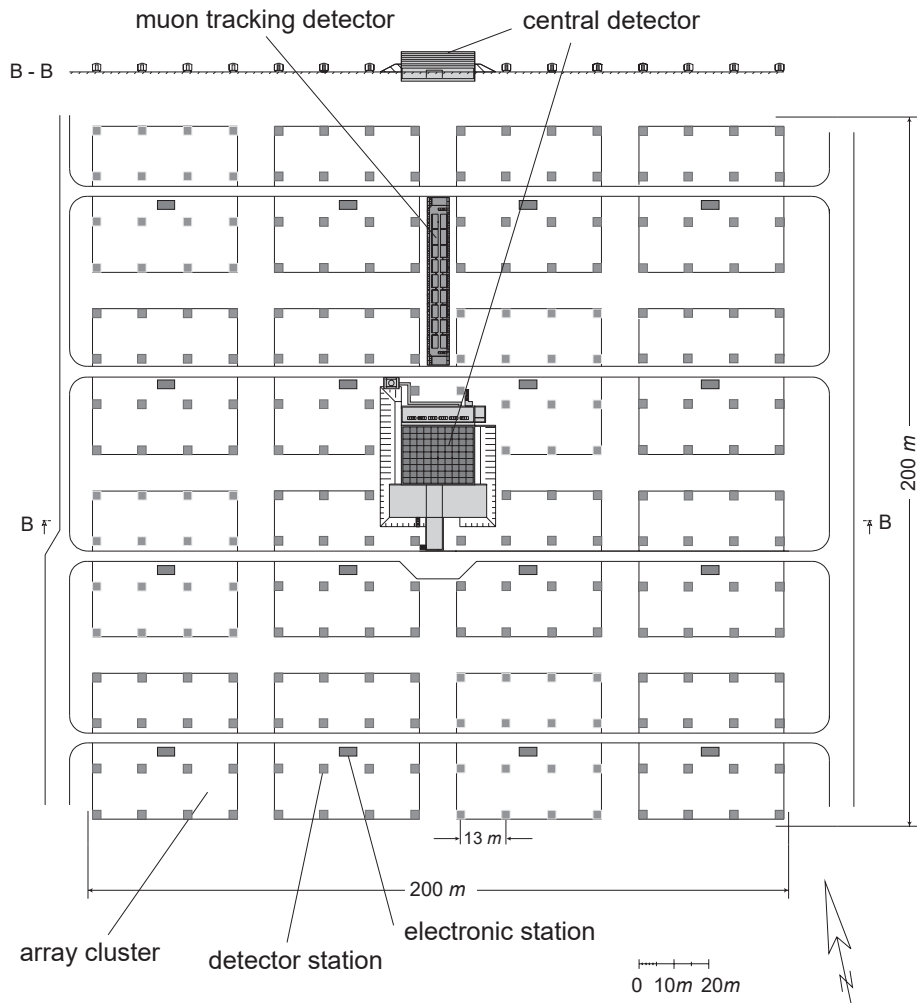


Figure 3.1: Schematic layout of the KASCADE experiment, from [6].

The central detector had the area of 320 m^2 and consisted of a hadron sampling calorimeter. This calorimeter was comprised of eight layers of iron absorber with nine layers of warm-liquid ionisation chambers scattered within. Below the third absorber plane a layer of plastic scintillators were used as a detector for studies of the extensive air shower time structure and to trigger the read-out. The finely segmented calorimeter is the main part of the central detector with 11000 chambers and 44000 read-out channels.

With the KASCADE-Grande extension, the experiment increased its sensitive range to the energies $10^{13} - 10^{19} \text{ eV}$. The experimental set-up of the extension also included the radio antenna field LOPES and the microwave experiment CROME [7]. The Grande array extended the effective area of KASCADE, and, therefore, its upper energy limit by a factor of ten. It consisted of 37 detector stations installed in an irregular triangular grid, covering the area of approximately 0.5 km^2 . The Grande array operated independently from the KASCADE array and measured the same parameters of the charged particle component.

The KASCADE experiment has shown [29] that the cause of the knee structure of the energy spectrum is caused by a steepening of the spectra of light elements

($Z < 6$). The KASCADE-Grande collaboration [30] has reported, see Figure 3.3, that such steepening occurs in the spectrum of heavier nuclei up to iron ($26 \geq Z > 13$) and measured the second knee at $8 \cdot 10^{16}$ eV, falling within the expected range of $4 \cdot 10^{16}$ eV to $1.2 \cdot 10^{17}$ eV. The Telescope Array Low Energy Extension (TALE) [3] describes the knees as a structure with a broad maximum centered at $\sim 10^{15.6}$ eV, a broad dip centered at $\sim 10^{16.2}$ eV and a second knee at $\sim 10^{17.04}$ eV, see Figure 3.2.

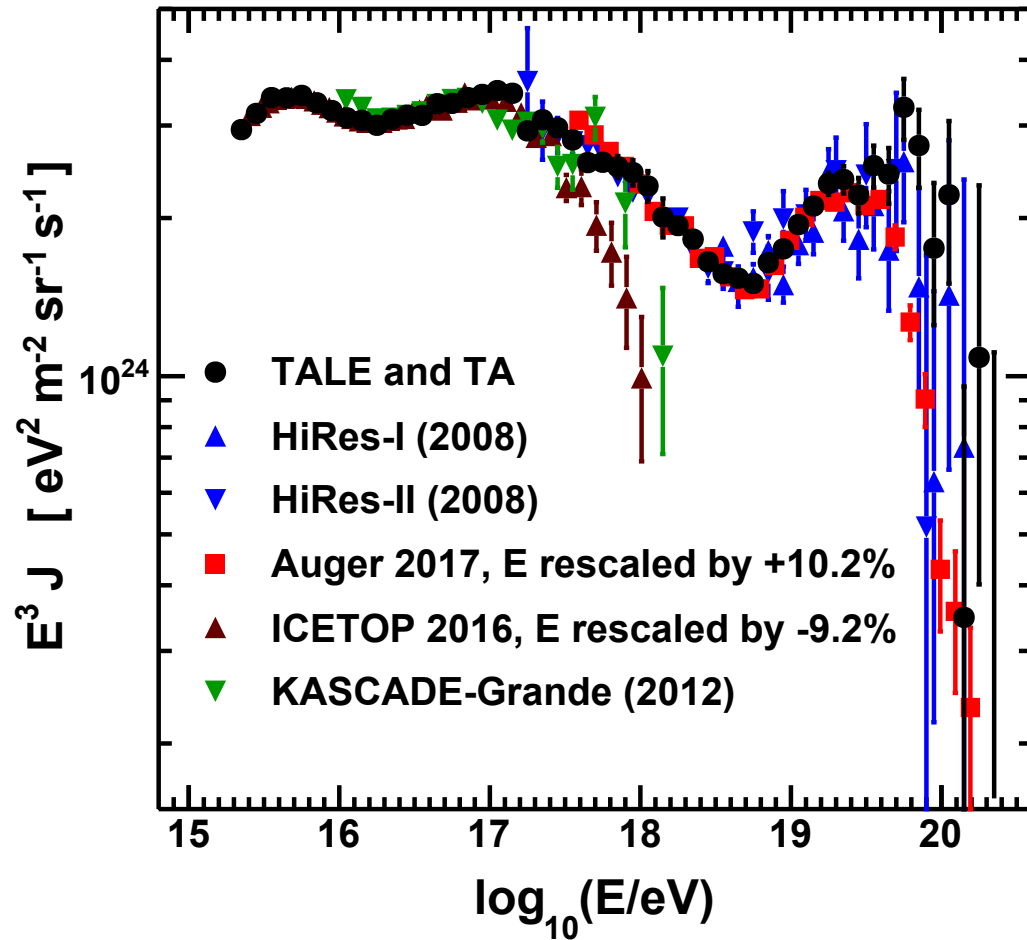


Figure 3.2: Cosmic Ray spectrum measured by TALE, TA, Auger, HiRes, IceTop, and KASCADE-Grande. The TALE and TA spectrum is obtained by combining the TALE and TA surface. The energy scale for Auger is raised by 10.2%, the energy scale for IceTop is lowered by 9.2%, from [3].

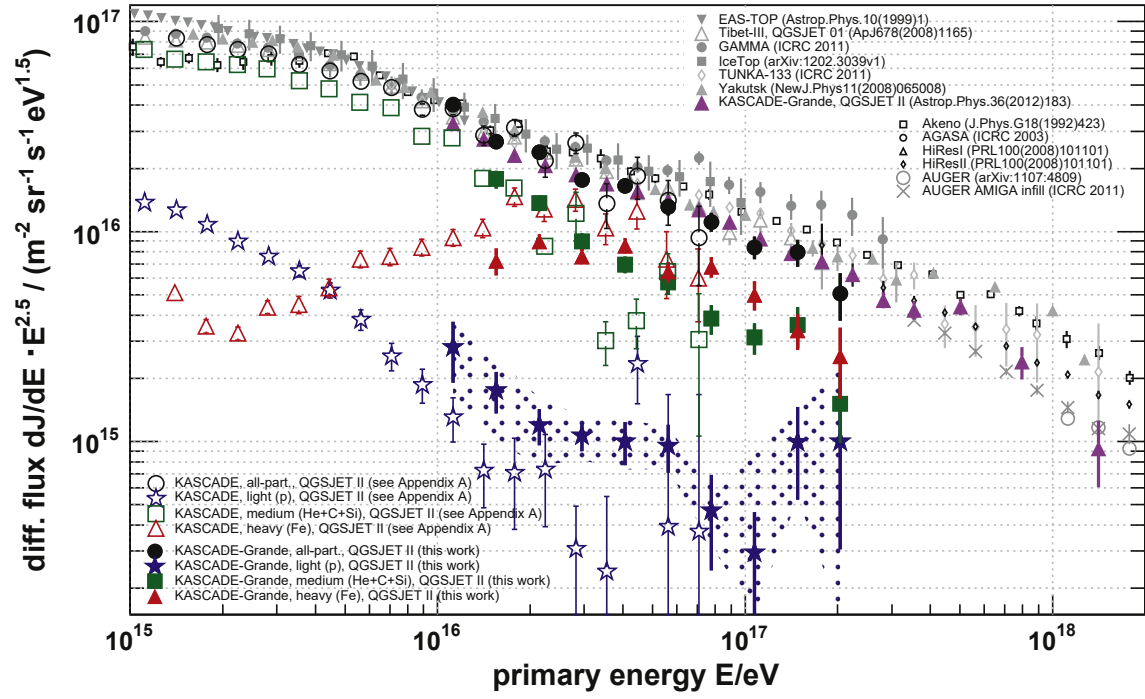


Figure 3.3: The all-particle spectrum based on an unfolding of KASCADE-Grande measurements, and the spectrum based on an unfolding of KASCADE measurements compared to spectra determined by other analysis methods of the KASCADE-Grande collaboration or other experiments. Additionally shown are some elemental spectra representing different mass groups. The error bars denote statistical uncertainties, error bands the systematic ones. From [31].

Chapter 4

KASCADE data and simulations

4.1 The KASCADE Cosmic ray Data Centre KCDC

The aim of the KCDC project (<https://kcdc.iap.kit.edu/>) is the installation and establishment of a public data centre for high-energy astroparticle physics based on the data of the KASCADE experiment, which collected more than 1.7 billion events [32] of which some 433 million survived all quality cuts. Physicists and the interested public can access the high-quality cosmic-ray data collected by KASCADE and KASCADE-Grande, achieved through regular internal quality tests and the application of 20 years of collective knowledge and experience of the KASCADE-Grande collaboration.

Open access includes free, unlimited access to the data that implies no change over time regarding the data source and access condition, as well as the publication of meta information and documentation. With KCDC, the first step was the publishing of the reconstructed physics data of the experiment along with the calibrated entry at each individual detector per event. This is not synonymous with raw data acquired by the detector, however, such data would require an in-depth knowledge on aspects of the detector system before the user can reasonably use the data. Instead, the reconstructed physics data are provided with the background information on the detector and the KASCADE experiment. While a user of the data centre can request a specific dataset, preselected datasets and simulations with pre- and post-LHC hadronic interaction models are available.

4.2 Current energy estimation formula

In order to obtain a formula for the energy estimation, CORSIKA simulations were used by applying the hadronic interaction model QGSJet-II 02 for laboratory energies above 200 GeV and the low energy model Fluka 2002_4 for the lower energies [33]. The energy range of the simulations was $10^{14} - 3 \cdot 10^{18}$ eV with zenith angles in the $0^\circ - 42^\circ$ range. The spectral index used was $\gamma = -2$ to save disk space and simulation time. This was later corrected for the real spectral index of the cosmic

rays in this range $\gamma = -2.7$.

For the parameterization, the air showers were divided into two zenith angle bins (from 0° to 18° and from 18° to 25°) with the same acceptance. Data in the energy range $10^{15} - 3.16 \cdot 10^{18}$ eV were divided to 15 logarithmically equidistant intervals, where mean values of the electromagnetic particle and muon distributions are determined. The achieved energy reconstruction formula is

$$\begin{aligned} \log_{10} E_{\text{rec}} = & 1.93499 + 0.66704 \cdot \log_{10} N_{\mu}^{\text{true}} + 0.07507 \cdot \log_{10}^2 N_e^{\text{true}} \\ & + 0.25788 \cdot \log_{10} N_e^{\text{true}} + 0.09277 \cdot \log_{10}^2 N_{\mu}^{\text{true}} \\ & - 0.16131 \cdot \log_{10} N_e^{\text{true}} \cdot \log_{10} N_{\mu}^{\text{true}}, \end{aligned} \quad (4.1)$$

where N_e^{true} is the true number of electrons on ground and N_{μ}^{true} is the true number of muons on ground, later corrected for attenuation. The comparison of the reconstructed energy and simulated energy can be seen in Figure 4.1.

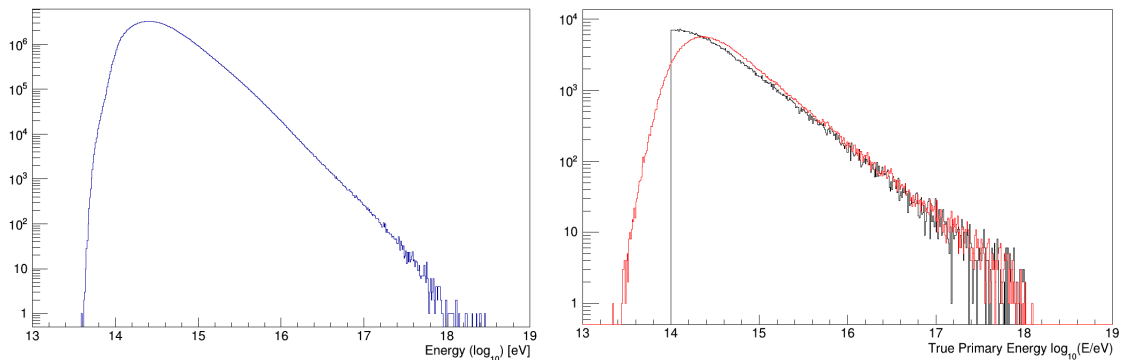


Figure 4.1: Left: The histogram of logarithm of energies reconstructed by the KASCADE experiment, see equation (4.1)[28]. Right: the histogram of the reconstructed (red) and the true (black) energies for simulated proton showers [33].

4.3 Data selection

In this work, we strive to use as much as possible the data and simulations provided by the KCDC. Both data and simulations contain information about the reconstructed number of muons N_{μ}^{rec} and electrons N_e^{rec} , reconstructed zenith angle θ^{rec} , reconstructed primary particle energy E^{rec} and lateral shape parameter s^{rec} , with the simulations also containing the true Monte Carlo variables: true number of muons N_{μ}^{MC} and electrons N_e^{MC} , true zenith angle θ^{MC} , true primary particle energy E^{MC} along with the primary type and hadronic interaction model used.

4.3.1 Additional simulations

The publicly available simulations do not have the longitudinal profile of the showers saved, which is necessary to obtain the calorimetric energy of the simulated showers.

For this, additional 60 000 showers were produced using the CORSIKA 7.64 code with the same settings as the publicly available KASCADE simulations [33], namely the low-energy model FLUKA 2011.2x.

The showers were generated with three hadronic interaction models - EPOS LHC, QGSJet-II 04 and Sibyll 2.3 along with the low-energy model FLUKA 2011.2x. Four primaries were used; protons and the nuclei of helium, nitrogen and iron. The simulated showers have ten fixed values of the zenith angle distributed uniformly in $\cos^2 \Theta_{\text{MC}}$; $\Theta_{\text{MC}} = 0^\circ, 12.3^\circ, 17.6^\circ, 21.8^\circ, 25.4^\circ, 28.6^\circ, 31.7^\circ, 34.5^\circ, 37.3^\circ, 40^\circ$ for five fixed primary energies $E^{\text{MC}} = 10^{15} \text{ eV}, 3.2 \cdot 10^{15} \text{ eV}, 10^{16} \text{ eV}, 3.2 \cdot 10^{16} \text{ eV}, 10^{17} \text{ eV}$.

4.3.2 KASCADE simulations

The publicly available simulations were created using the simulation program CORSIKA and the hadronic interaction models EPOS LHC, QGSJet-II 04 and Sibyll 2.3. The detector response is simulated using the program CRES, from which the air shower is reconstructed, using the program KRETA. The spectral index of the simulated energy spectrum is $\gamma^{\text{MC}} = -2$, which we correct to $\gamma^{\text{KASCADE}} = -2.7$ as was done with the original energy estimation formula. The primary particles used were protons and the nuclei of helium, carbon and iron. We use quality cuts recommended by the KCDC simulation manual: $\log N_\mu^{\text{rec}} \geq 4$, $\log N_e^{\text{rec}} \geq 4.4$, $1.3 \geq s^{\text{rec}} \geq 0.6$ and $\theta^{\text{rec}} \leq 25^\circ$. The zenith cut is applied for the compatibility with the current reconstruction formula, which was derived using the same zenith range.

4.3.3 KASCADE data

For the detected data published by KCDC, we use NABOO 2.0 version of released preselected showers from runs 877 – 4683 containing 143 116 296 events detected in the time period 8.5.1998 — 20.12.2003. The detailed information about this dataset is available on the KCDC website on the page https://kcdc.iap.kit.edu/static/pdf/kaos_datashop/KASCADE_ReducedData_runs_0877-4683_ROOT.pdf. We again use quality cuts: $\log N_\mu^{\text{rec}} \geq 4$, $\log N_e^{\text{rec}} \geq 4.4$, $1.3 \geq s^{\text{rec}} \geq 0.6$ and $\theta^{\text{rec}} \leq 25^\circ$.

Chapter 5

New energy estimation from KASCADE data

One of the main goals of the measurements of the extensive air showers is the determination of the energy and mass of the primary particle and, consecutively, the energy spectrum of the cosmic rays [28][33]. The hadronic interactions taking place in the atmosphere are burdened by uncertainties caused, among other phenomena, by fluctuations in the shower size, rendering the determination of energy and mass rather challenging.

One of the main flaws of the interpretation of the ground detection of extensive air showers is the extrapolation of properties of particle interactions measured at accelerators [34]. The beam energies attained at the proton-proton collisions at LHC reach 13 TeV at the centre-of-mass system, which is comparable to the first interaction in the atmosphere of a cosmic ray with the primary energy $\approx 10^{17}$ eV. The measurements at accelerators also cover lower pseudorapidity regions than those covered by the majority of the energy flux of the first interactions of cosmic rays with the atmospheric nuclei.

The energy not deposited in the atmosphere is called the invisible energy and is carried by muons and neutrinos. It is a considerable source of systematic uncertainties in the energy spectrum below ≈ 1 EeV, based on the energy scale inferred from the optical detection technique [3] [35]. We apply a data-driven method to obtain the invisible energy from the publicly available data of the KASCADE experiment, see Chapter 4.3.3, based on the approach used by the Pierre Auger Observatory [36]. The inconsistencies caused by the extrapolation of LHC data to describe air showers, namely the muon component of the shower, which are higher at ultra-high energies [37], were also observed at the KASCADE-Grande [38]. To decrease the systematic uncertainties caused by the invisible energy and accelerator data extrapolation, we attempt to reconstruct the energy of the primary cosmic ray by correcting the calorimetric energy for the invisible energy [36]. By calorimetric energy we mean the deposited energy of the shower, which can be observed by the production of faint isotropic fluorescence and collimated Cherenkov light during the propagation of secondary cosmic rays towards the Earth surface [3] [35]. Since the KASCADE experiment measured the electromagnetic and muonic components independently,

both observables can be used to perform a transformation matrix in order to convert the number of electrons and muons to the energy of the primary particle while taking the zenith angle into account. However, the biases of the shower energy estimated using this formula can be decreased by introducing an additional parameter, the lateral shape parameter, related to the age of the air shower, s^{rec} [34].

The lateral shape parameter is connected with the equations for the lateral distribution of electrons and photons in an approximation of cascade theory [39]. The solution of the cascade equations is a function of the core distance R scaled with Molière units R_M and the shower age parameter s^{rec} , which characterises the cascade development. The Greisen's approximation of Nishimura and Kamata solution is

$$f\left(\frac{R}{R_M}\right) \propto \left(\frac{R}{R_M}\right)^{s^{\text{rec}}-2} \left(1 + \frac{R}{R_M}\right)^{s^{\text{rec}}-4.5}, \quad (5.1)$$

and is known as the NKG-function [40].

5.1 Invisible energy

We derive the universal relation between the invisible energy and the number of muons measured at ground by the KASCADE experiment. However, the simulations publicly available at KCDC do not have the longitudinal profile of the showers saved, which is necessary to obtain the calorimetric energy of the simulated showers. For this, we use the additional 60 000 showers containing the longitudinal profile of the shower, see Section 4.3.1. These are the same additional simulations used in [34]. The additional CORSIKA showers were used to find a universal relation between the invisible energy of the Monte Carlo simulations $E_{\text{inv}}^{\text{MC}}$ and the simulated number of muons N_{μ}^{MC} , which is obtained as a sum of all muons above 100 MeV reaching the ground level. For each of the ten fixed zenith angles, the function

$$E_{\text{inv}}^{\text{MC}}(N_{\mu}^{\text{MC}}) = C \cdot (N_{\mu}^{\text{MC}})^{\delta} \quad (5.2)$$

was fitted for each model and primary separately and then for all models and primaries combined. An example for the zenith angle $\Theta_{\text{MC}} = 17.6^\circ$ is shown in Figure 5.1 and the obtained parameters C and δ are shown in the left and right panels of Figure 5.2, respectively.

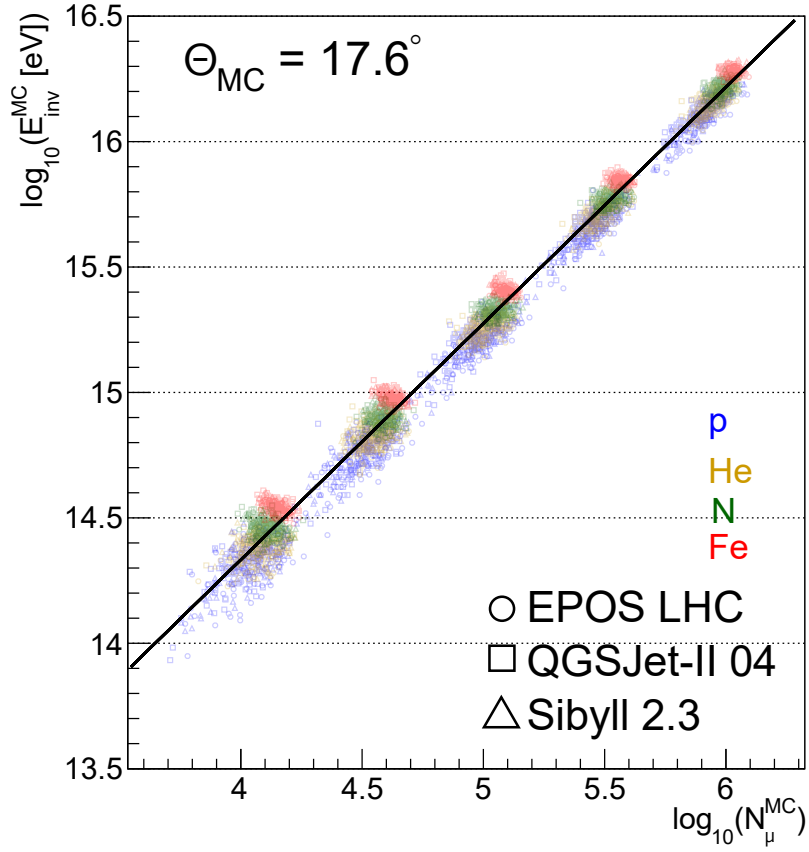


Figure 5.1: Calibration of the invisible energy with respect to the number of muons for $\theta_{MC} = 17.6^\circ$ along with the fitted function in Eq. (5.2) for all models and primaries.

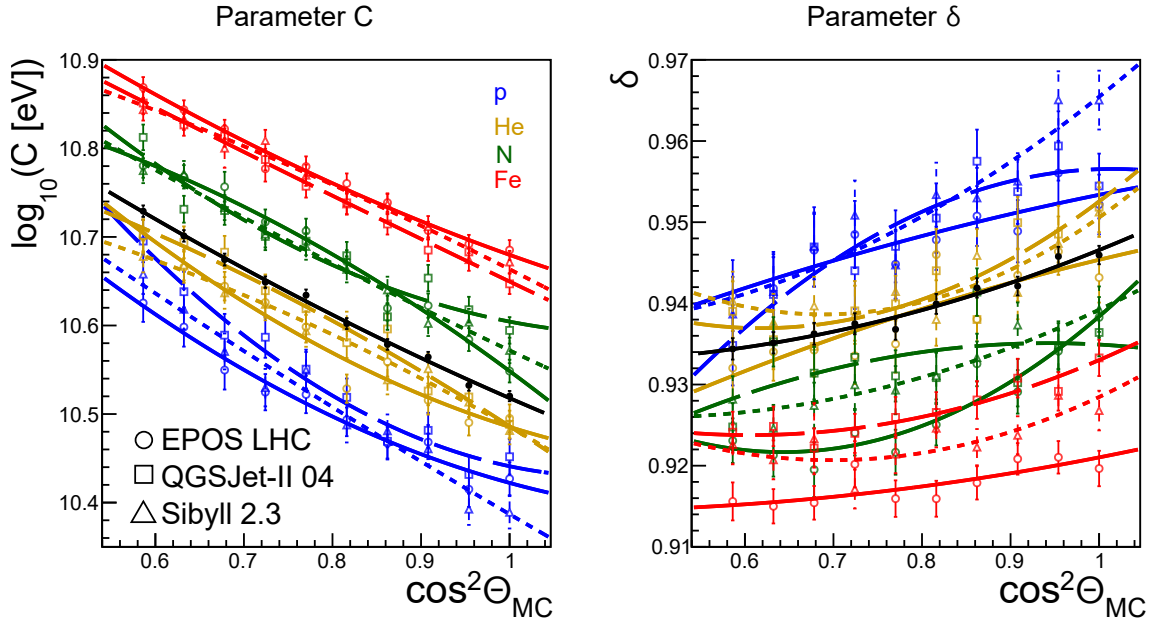


Figure 5.2: The evolution of the fitted parameter C (left) and δ (right) from the Eq. (5.2) with respect to $\cos^2 \theta_{MC}$ for each model and primary along with all models and primaries combined (black) using a polynomial of the second order.

5.2 Calorimetric energy

The calibration of the calorimetric energy was applied to KASCADE simulations provided by KCDC, see Section 4.3.2. We use KASCADE simulations created using the simulation program CORSIKA and the hadronic interaction programs EPOS LHC, QGSJet-II 04 and Sibyll 2.3. We use quality cuts recommended by the KCDC simulation manual, namely the cut for the zenith angle being $\leq 25^\circ$, since the Eq. (4.1) was derived for these zenith angles, and $s = 0.6 - 1.3$, $\log_{10} N_e \geq 4.4$, $\log_{10} N_\mu \geq 4$. The derived general relationship between the invisible energy and the number of muons, which can be seen in Figure 5.2, is used to establish the calorimetric energy per shower for given hadronic interaction model and primary as $E_{\text{Cal}}^{\text{MC}} = E^{\text{MC}} - E_{\text{Inv}}(N_\mu^{\text{MC}}, \Theta_{\text{MC}})$.

We investigate the dependence of this calorimetric energy on the number of charged particles transformed to the zero zenith angle. We take the number of charged particles transformed to the zero zenith angle as the sum of the number of electrons and the number of muons both transformed to the zero zenith angle. This transformation to the zero zenith angle was performed by analysing the behaviour of the number of electrons and the number of muons with increasing zenith angle using the additional KASCADE simulations, as the fixed zenith angles minimise the systematic uncertainties due to the binning. The relation between the number of muons and the zenith angle is depicted in the left panel of Figure 5.3, the relation between the number of electrons and the zenith angle in the right panel of Figure 5.3.

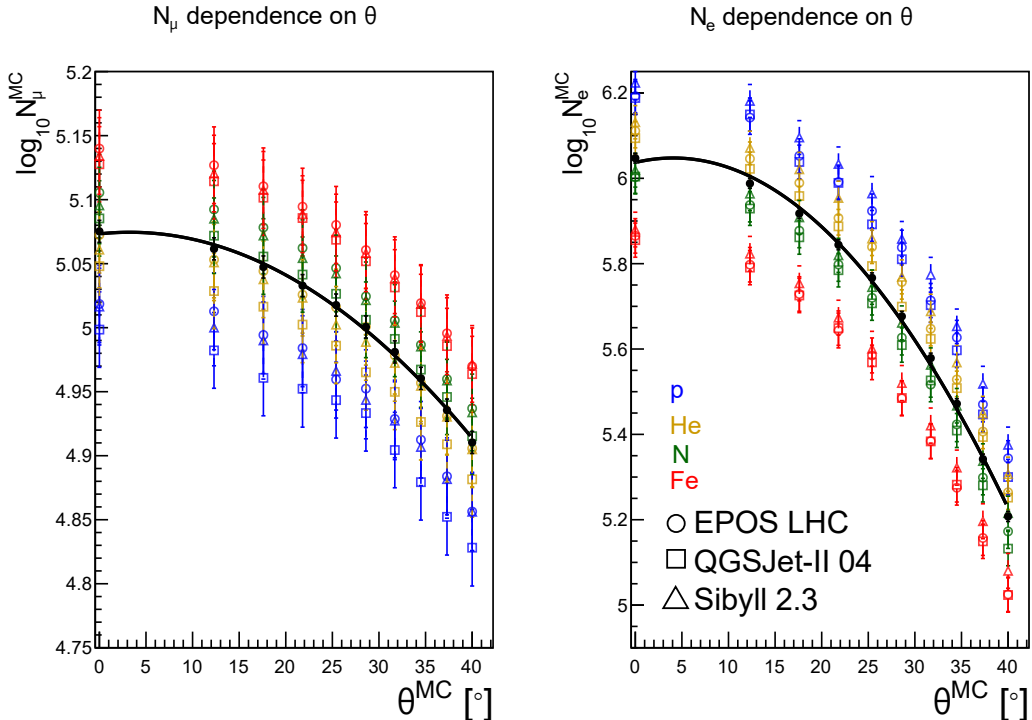


Figure 5.3: The dependence of the number of muons (left) and electrons (right) with respect to the zenith angle for each model and primary, along with the fitted polynomial of the second order for all models and primaries (black).

We selected the showers of all hadronic interaction models and primaries in different bins in the lateral shape parameter in the range $1.3 \geq s^{\text{rec}} \geq 0.6$ with the bin size of 0.05. The range was chosen to have enough data in a given bin for the fit to converge. For each bin, the function

$$E_{\text{Cal}}^{\text{MC}} (N_{\text{ch}}^{\text{MC}} (0^\circ)) = D \cdot (N_{\text{ch}}^{\text{MC}} (0^\circ))^\omega \quad (5.3)$$

was fitted for each model and primary separately and then for all models and primaries combined. An example for the lateral shape parameter bin $s^{\text{rec}} = 0.9 - 0.95$ is shown in Figure 5.4, the obtained parameters D and ω in the left and right panels of Figure 5.5, respectively.

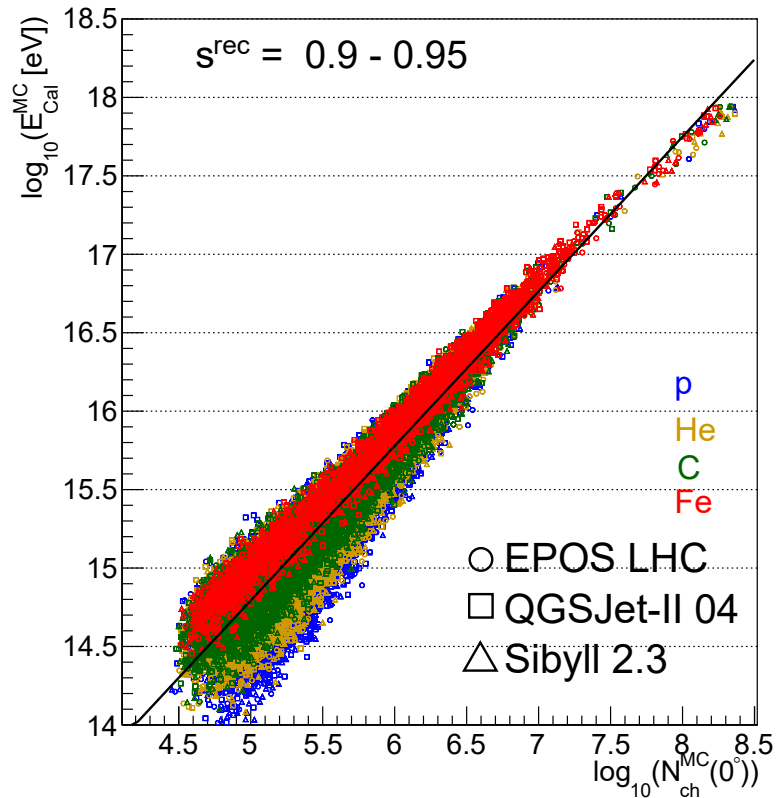


Figure 5.4: Calibration of the calorimetric energy with respect to the number of charged particles transformed to the zero zenith angle for $s^{\text{rec}} = 0.9 - 0.95$ along with the fitted function in Eq. (5.3).

We correct for the evolution of s^{rec} , and consequently X_{max} , with energy using a polynomial of the fifth order. The difference can be seen in the left panel of Figure 5.6, and the smoothed dependence in the right panel of Figure 5.6.

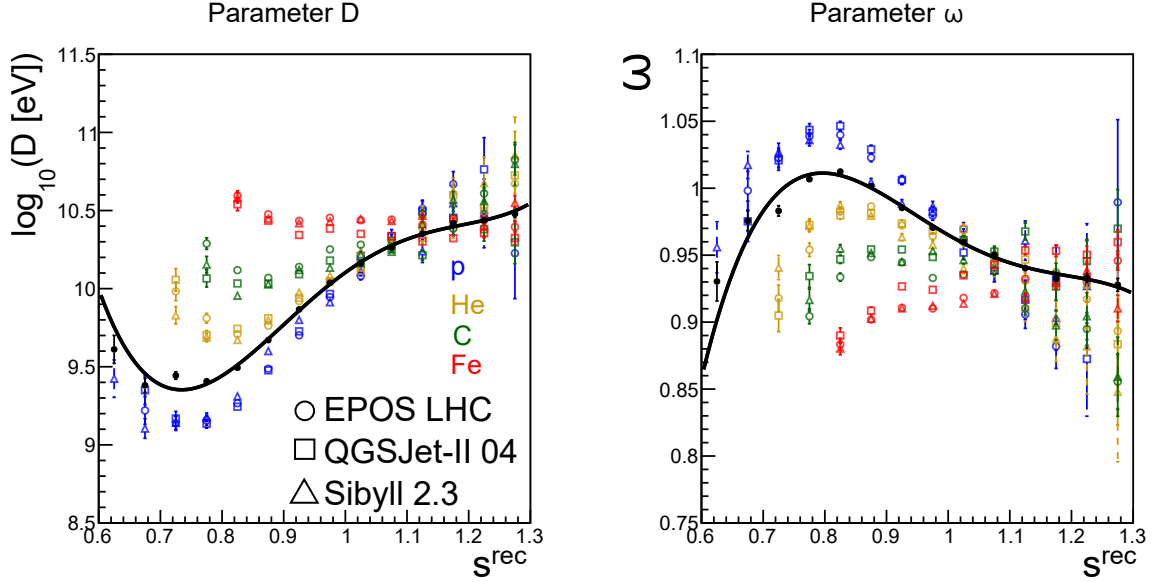


Figure 5.5: The evolution of the fitted parameter D (left) and ω (right) from Eq. (5.3) with respect to the age parameter s^{rec} for each model and primary along with all models and primaries combined (black) fitted by the polynomial of the fourth order.

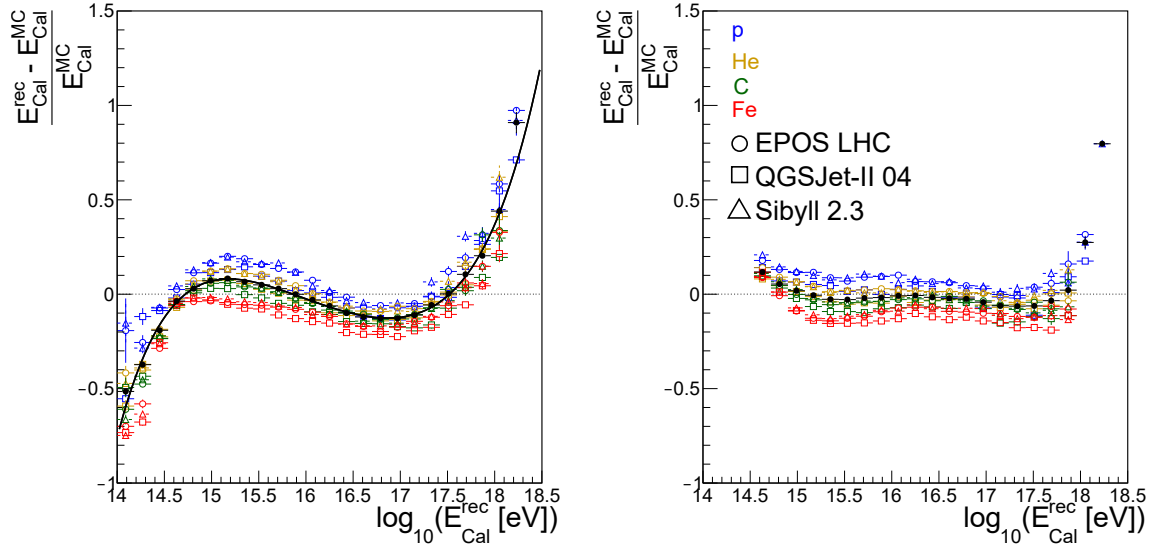


Figure 5.6: **Left:** The relative difference between $E_{\text{Cal}}^{\text{rec}} = E^{\text{MC}} - C \cdot (N_{\mu}^{\text{MC}})^{\delta}$ and $E_{\text{Cal}}^{\text{MC}} = D \cdot (N_{\text{ch}}^{\text{MC}}(0^{\circ}))^{\omega}$, fitted by a polynomial of the fifth order. **Right:** The difference after the application of the correction function shown by the black line in the left panel.

5.3 Comparison of energy estimation formulae

The derivation of the universal relation between the invisible energy and the number of muons and the calibration of the calorimetric energy were done either on

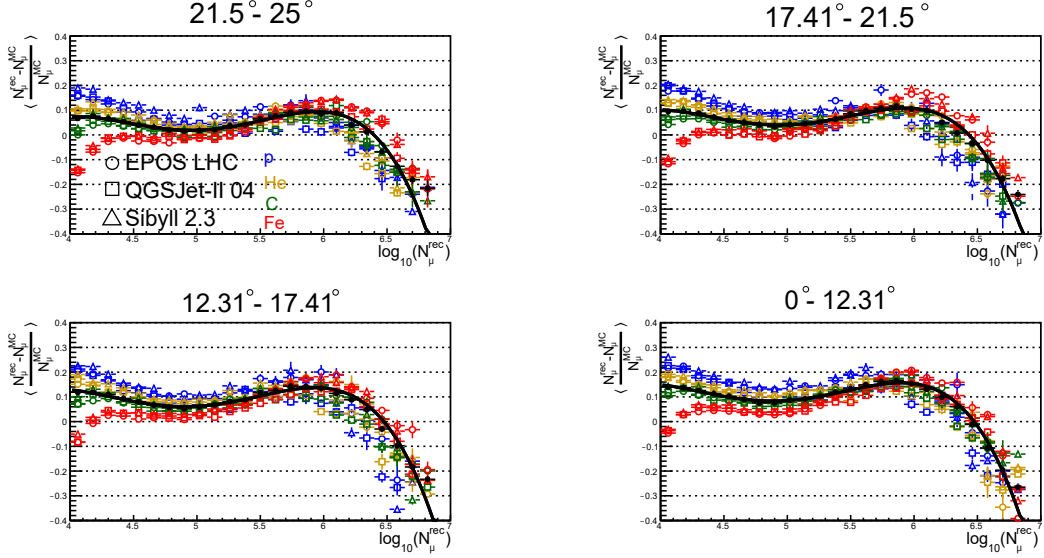


Figure 5.7: The evolutions of average relative differences between the reconstructed number of muons N_{μ}^{rec} and the true number of muons N_{μ}^{MC} with the reconstructed number of muons for four zenith angle bins for each model and primary, along with the fitted polynomial of the fifth order for all models and primaries (black).

pure Monte Carlo variables or variables derived from pure Monte Carlo variables. To meaningfully compare the energy estimators, we must correct for the detector response, meaning assess the biases of the reconstructed number of electrons and muons. We further divide the dataset into four zenith angle bins, equidistant in $\cos^2 \theta^{\text{MC}}$. The biases of the muon number can be seen in Figure 5.7, the biases of the electron number in Figure 5.8. The biases were fitted with a polynomial of the fourth order for all models and primaries. The evolution of the parameters of these polynomials can be seen in Table A.1 in Appendix, with the electron dependencies in the first five rows and the muon dependencies in the sixth to tenth rows. We keep this binning for next analysis.

The resulting energy reconstruction is summarised as follows:

1. For a shower in the $\cos^2 \theta^{\text{rec}}$ bin, where θ^{MC} is the reconstructed zenith angle, the detector response for the number of muons and the number of electrons is corrected using the formula

$$N_{\mu,e}^{\text{corr}} = \frac{N_{\mu,e}^{\text{rec}}}{f_{\mu,e}^{\text{corr}}(N_{\mu,e}^{\text{rec}}) + 1}, \quad (5.4)$$

where $f_{\mu,e}^{\text{corr}}(N_{\mu,e}^{\text{rec}}) = \sum_{i=0}^4 p_i^{\mu,e} (N_{\mu,e}^{\text{rec}})^i$ is a polynomial of the fourth order. The parameters $p_i^{\mu,e}$ are listed in Table A.1 in Appendix.

2. The logarithm of the invisible energy is calculated using the formula

$$\log E_{\text{Inv}}^{\text{rec}} = \log C(\cos \theta^{\text{rec}}) + \log N_{\mu}^{\text{corr}} \cdot \delta(\cos \theta^{\text{rec}}). \quad (5.5)$$

The parameters of this formula are in Eq. (A.1) in Appendix.

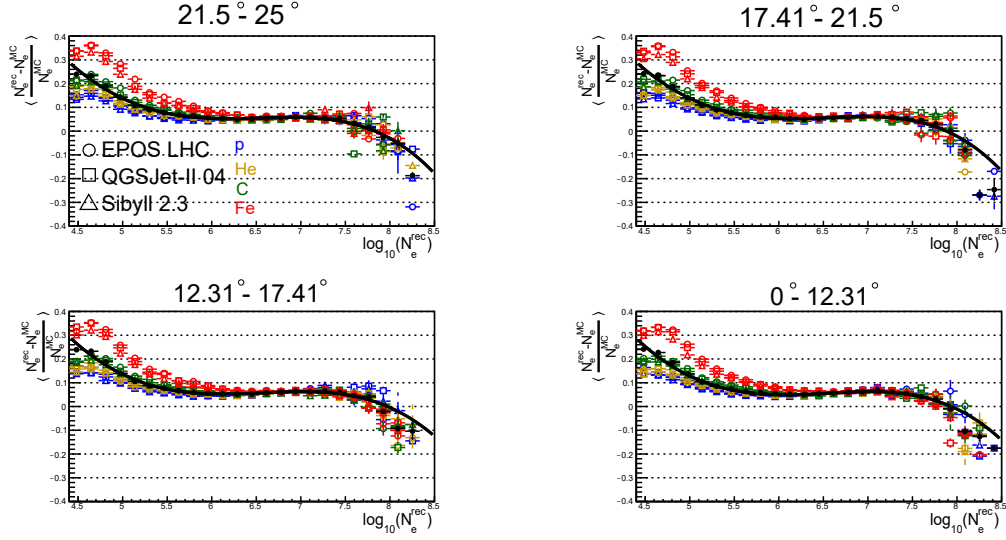


Figure 5.8: The evolution of average relative differences between the reconstructed number of electrons N_e^e and the true number of muons N_μ^{MC} with the reconstructed number of electrons for four zenith angle bins for each model and primary, along with the fitted function for all models and primaries (black).

3. The number of charged particles transformed to the zero zenith angle is calculated using the formula

$$N_{\text{ch}}(0^\circ) = N_\mu^{\text{corr}}(0^\circ) + N_e^{\text{corr}}(0^\circ), \quad (5.6)$$

The parameters of these formulae are in Eq. (A.2) in Appendix.

4. Then, the calorimetric energy is estimated as

$$\log E_{\text{Cal}} = \log D(s^{\text{rec}}) + \log N_{\text{ch}}(0^\circ) \cdot \omega(s^{\text{rec}}). \quad (5.7)$$

The parameters of these formulae are in Eq. (A.2) and (A.3), respectively, in Appendix.

5. Then, the logarithm of the calorimetric energy is corrected for the evolution of the shower age with energy, see Figure 5.6, using the formula

$$E_{\text{Cal}}^{\text{corr}} = \frac{E_{\text{Cal}}}{p_5(\log E_{\text{Cal}}) + 1}. \quad (5.8)$$

The parameters of this formula are in equation (A.4) in Appendix.

6. Finally, the invisible energy and the corrected calorimetric energy are summed, resulting in the new energy estimate

$$E_{\text{new}} = E_{\text{Inv}}^{\text{rec}} + E_{\text{Cal}}^{\text{Corr}}. \quad (5.9)$$

The comparison of the biases for the two energy estimation formulae with respect to the simulated energy is shown in Figure 5.9 for the hadronic interaction model

EPOS LHC. The comparison of the biases for the model QGSJet-II 04 can be seen in Figure A.1 in Appendix, for the model Sibyll 2.3 in Figure A.2 in Appendix. One can see that the standard energy reconstruction shows a dependence on the primary energy. On the other hand, the new energy reconstruction is more monotonous with respect to the increasing primary energy. As the primary particle energy is unknown upon detection, this consistency in biases is favourable, especially in studies of the cosmic-ray energy spectra.

The resolution of the energy estimators with respect to the simulated energy is plotted in Figure 5.10 for the hadronic interaction model EPOS LHC. The resolution for the model QGSJet-II 04 can be seen in Figure A.3 in Appendix, for the model Sibyll 2.3 in Figure A.4 in Appendix. It should be pointed out that the resolution is improved in the new energy reconstruction method, with decreased differences between primaries. The variable $\sigma \left(\frac{E^{\text{new}} - E^{\text{MC}}}{E^{\text{MC}}} \right)$ decreases with rising energy, as expected for more stations with a triggered signal in the shower reconstruction.

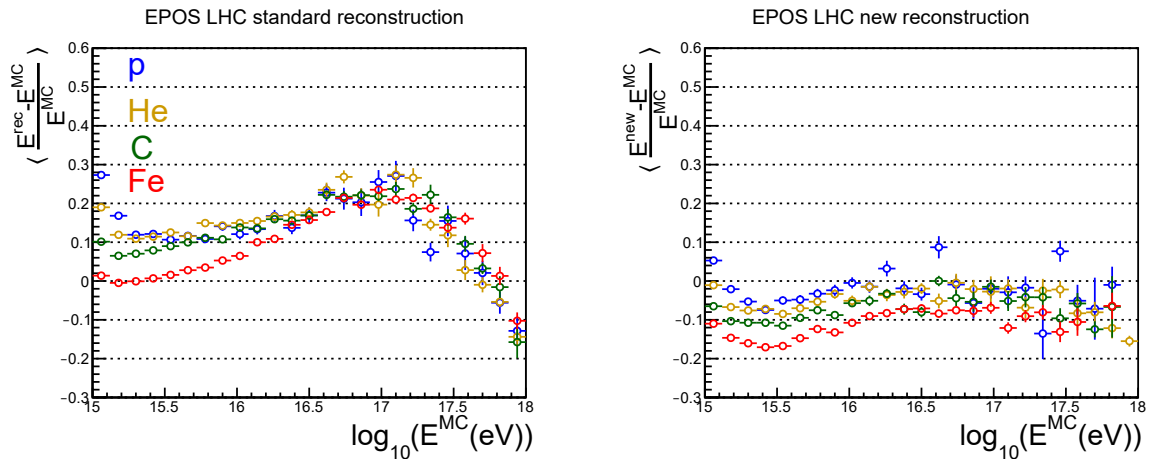


Figure 5.9: The energy evolutions of average relative differences between the reconstructed and true shower energies for the hadronic interaction model EPOS LHC estimated using the KASCADE formula (**left**) and using the new energy calibration (**right**), see Eq. (5.4) to (5.9).

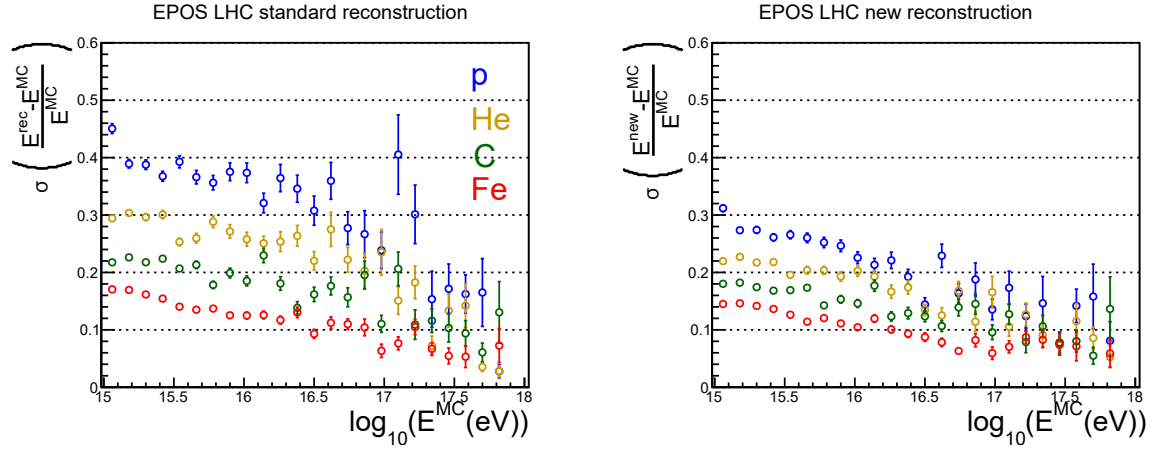


Figure 5.10: The energy evolutions of the standard deviation of relative differences between reconstructed and true shower energies for the hadronic interaction model EPOS LHC estimated using the KASCADE formula (**left**) and using the new energy calibration (**right**). Bins with less than 3 events are not included.

It is also useful to address the biases with respect to the reconstructed energy, as upon detection, we do not know the particle's true energy. The comparison between the two energy estimation formulae is shown in Figure 5.11 for the hadronic interaction model EPOS LHC. The comparisons for the models QGSJet-II 04 and Sibyll 2.3 are in Figure A.5 and Figure A.6 in Appendix, respectively. As was the case for Figure 5.9, the standard energy reconstruction shows a dependence on the primary energy, while the new energy reconstruction is more monotonous. The standard reconstruction also shows larger differences between primaries, which the new energy reconstruction decreases. Since the primary particle type and energy are unknown upon detection, the monotonous nature of the biases of the new energy reconstruction is preferred.

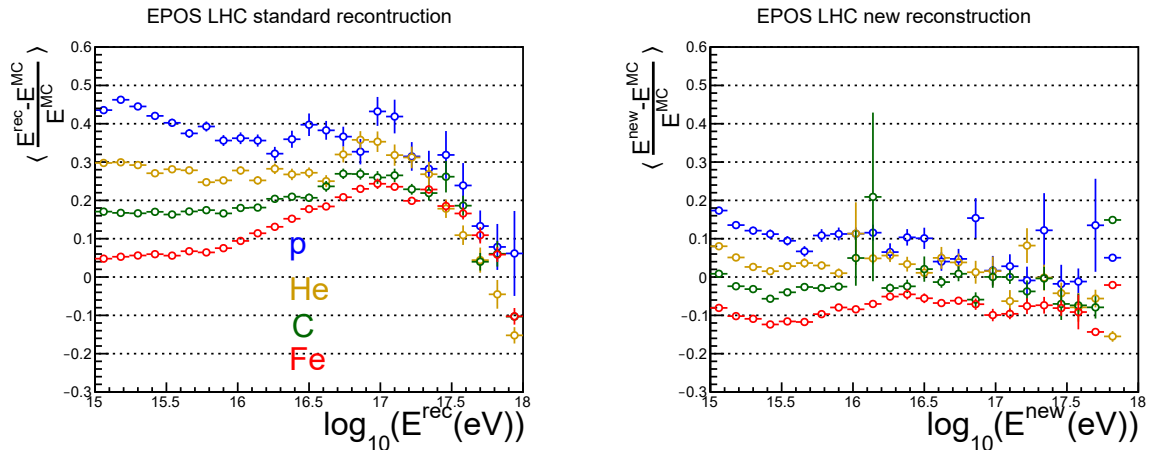


Figure 5.11: The energy evolutions of average relative differences between the reconstructed and true shower energies for the hadronic interaction model EPOS LHC dependent on reconstructed energies estimated using the KASCADE formula (**left**) and using the new energy calibration (**right**), see Eq. (5.4) to (5.9) in Section 5.3.

Chapter 6

Consequences of new energy calibration

6.1 Energy dependence of muon number

Measurements of KASCADE-Grande on the muon size in high energy air showers have provided evidence that the actual attenuation length of shower muons in the atmosphere is larger than the expectations from the hadronic interaction models, such as QGSJet-II 04, EPOS LHC and Sibyll 2.3 [41]. This discrepancy may be related to an inaccurate description of the shower muon content with atmospheric depth by hadronic interaction models. In particular, studies analysing the muon content in extensive air showers with primary energies above 10 PeV point out an excess in the measured number of shower muons over expectations, which seems to increase with the primary energy [37]. We plot the dependence of the number of muons as a function of standard and new energy in Figure 6.1.

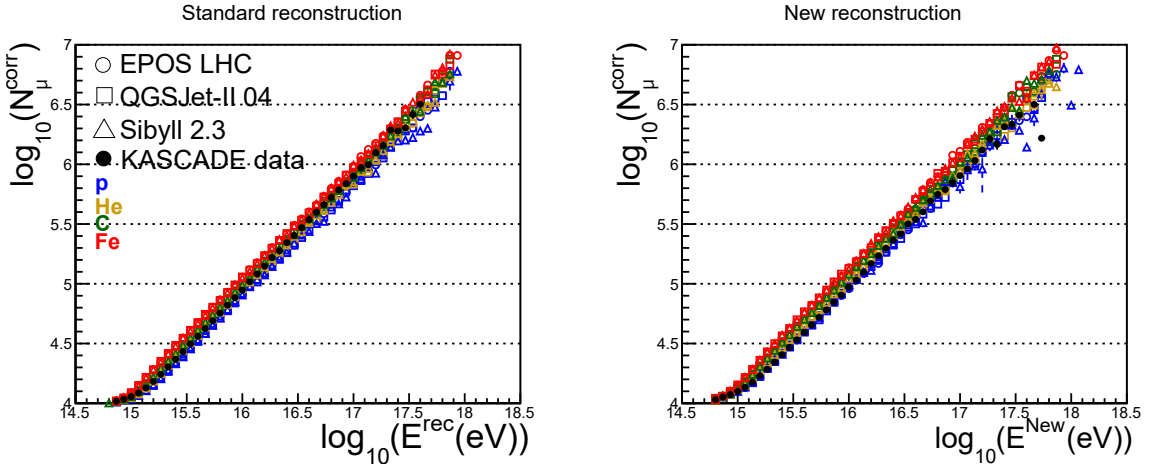


Figure 6.1: **Left:** Energy evolution of the corrected number of muons for standard KASCADE reconstruction, **right:** energy evolution of the corrected number of muons for the new energy reconstruction. Predictions for different hadronic interaction models and primaries are compared with the KASCADE data.

To compare the muon densities derived from the current and new energy calibration, we introduce the z parameter [42], defined as

$$z = \frac{\log(N_{\mu}^{\text{det}}) - \log(N_{\mu_{\text{p}}}^{\text{det}})}{\log(N_{\mu_{\text{Fe}}}^{\text{det}}) - \log(N_{\mu_{\text{p}}}^{\text{det}})}, \quad (6.1)$$

where N_{μ}^{det} is the reconstructed muon number, and $N_{\mu_{\text{p}}}^{\text{det}}$, $N_{\mu_{\text{Fe}}}^{\text{det}}$ is the simulated muon number for protons or iron nuclei, respectively. The reconstructed muon number was corrected for the bias, see Figure 5.7 and Figure 5.8. The relation holds $z = 0$ for purely proton showers, $z = 1$ for purely iron showers. The relation between the z parameter and the atomic weight A is

$$\langle \ln A \rangle = z \cdot \ln 56. \quad (6.2)$$

We use the GSF model [12] as a reference model to obtain $\langle \ln A \rangle$, re-scaled in energy by a factor of 0.88 to correctly describe the modeled mass evolution for the KASCADE experiment. We plot the resulting values of the z parameter for the old and new energy reconstruction in Figure 6.2

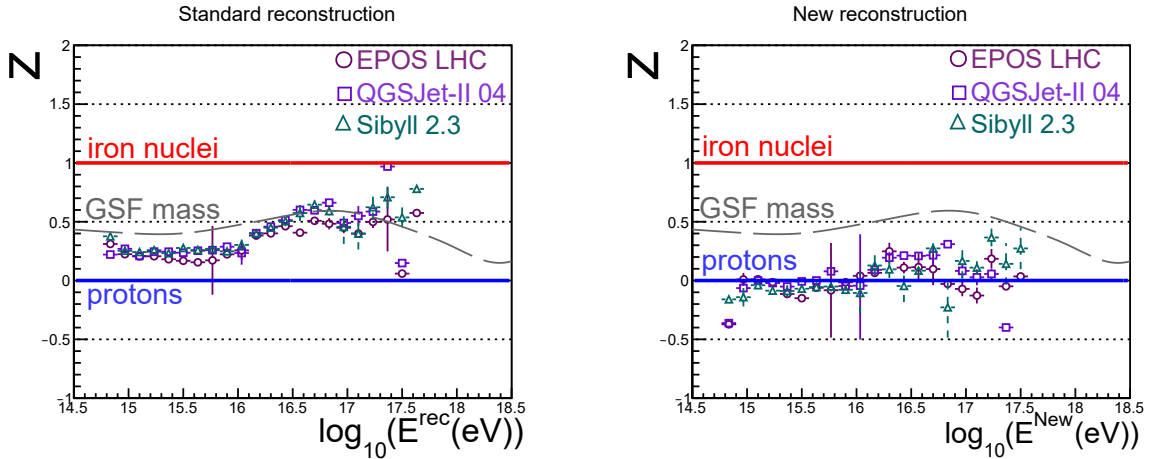


Figure 6.2: The z parameter, see Eq. (6.2), as a function of the reconstructed energy using the standard KASCADE reconstruction (**left**) and using the new energy reconstruction (**right**) for three different hadronic interaction models, with lines indicating a purely proton and purely iron showers.

Contrary to the previously discussed discrepancies between the models and the measurements, it seems that the KASCADE experiment actually detects slightly less than the predicted amount of muons on ground. This is apparent in the left panel in Figure 6.2, where the data points tend to fall between the GSF model prediction and the pure proton shower. The data copy the shape of the GSF model prediction, except the high-energy region, where the fluctuations are too high.

The new energy calibration underestimates the number of muons, dragging the KASCADE data points in the right panel in Figure 6.1 to the proton predictions. The

data points once again copy the shape of the GSF model prediction in the right panel in Figure 6.2.

6.2 Invisible energy fraction

The invisible energy is closely connected to the number of muons, and in our energy estimation, is directly derived from it. We plot the fraction of the invisible energy to the total shower energy as a function of the logarithm of calorimetric energy for the standard and new energy reconstructions in Figure 6.3. We also plot the predictions for protons and iron nuclei, produced by CONEX 6.40 for zenith angles within 25° [43]. These predictions are used to plot the GSF model prediction.

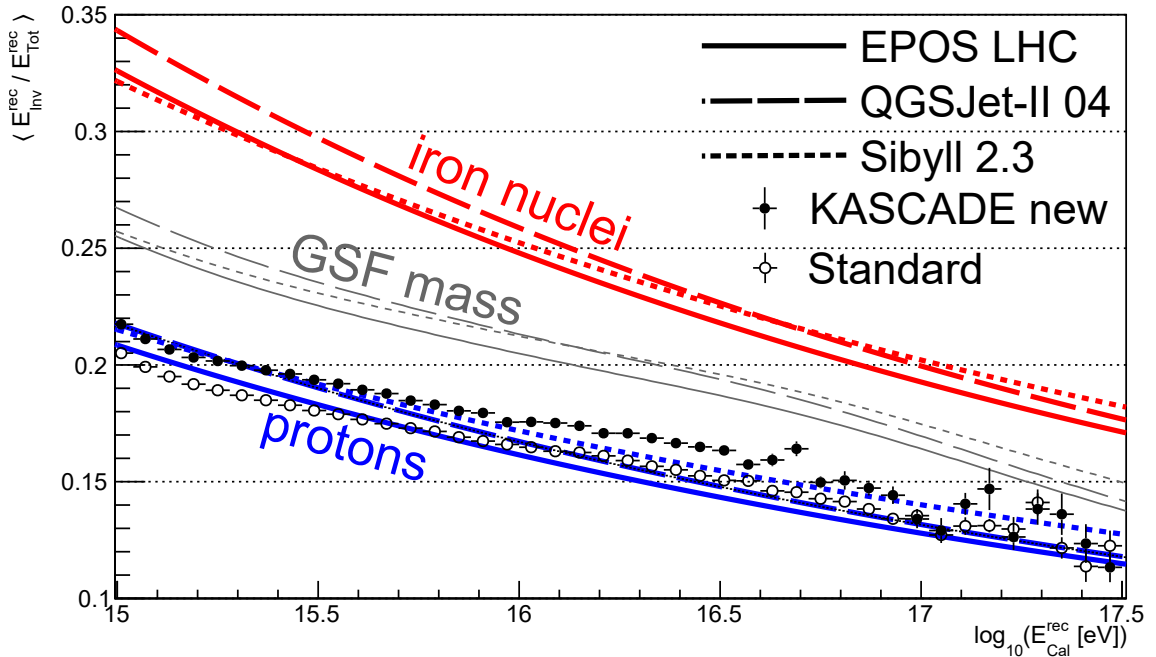


Figure 6.3: Invisible energy as a fraction of total shower energy depending on the logarithm of the calorimetric energy along with CONEX 6.40 predictions for protons and iron nuclei and the GSF model compared to the KASCADE new estimator formula (full points) and the standard one (open marks), as $E_{Cal}^{Std} = E_{Tot}^{Std} - E_{Inv}^{rec}$.

We see several break points in the data, namely in $\log_{10}(E_{Cal}^{corr} [eV]) \approx 15.2, 16,$ and 16.6 , suggesting possible changes in the energy evolution of the mass spectrum. The standard reconstruction energy was not corrected for bias, which can be seen in Figure 5.9 for true energy and Figure 5.11 for the reconstructed energy. This may influence the validity of the comparison between the invisible energy fraction of the standard and new energy reconstruction, seeing as the standard energy reconstruction biases are larger than zero, meaning that the standard reconstruction overestimates the true value of the energy. This means that the true standard invisible energy fraction could be higher than plotted, and may be higher than the invisible energy fraction as predicted by the new energy reconstruction, as showed in

[44]. Since the biases of the standard reconstruction method are energy dependent, the shape of the data points may also change if corrected for bias.

6.3 Mass-dependent energy spectrum

The energy spectrum of cosmic rays follows roughly a power law behaviour over many orders of magnitude in energy [31]. Still, there are few observable structures, see Section 1.1.2. In 1958, a distinct steepening in the electron size spectrum measured for extensive air showers was observed by Kulikov and Khristiansen at a few PeV [45]. It was three years later concluded by Peters [46] that the position of this kink, called the knee, will depend on the atomic number of the cosmic-ray particles if their acceleration is correlated to the magnetic fields. This means that the spectra of lighter and heavier cosmic rays exhibit knee structures at energies proportional to their charges.

The KASCADE results [29] have proved that the knee in the all-particle spectrum at about 5 PeV corresponds to a decrease of flux observed for light cosmic-ray primaries. This result was achieved by means of an unfolding analysis disentangling the convoluted energy spectra of five mass groups from the measured two-dimensional shower size distribution of electrons and muons at the observation level. In this thesis we observe the changes in the energy spectrum in the range of $10^{15} \text{ eV} < E < 10^{18} \text{ eV}$, where the relevant structures are the knee ($E \sim 10^{15} \text{ eV}$) and the second knee ($E \sim 10^{17} \text{ eV}$). In the TALE (Telescope Array Low Energy Extension) [3] energy spectrum the knee appears as a broad maximum centered at $10^{15.6} \text{ eV}$. There is a broad dip centered at $10^{16.2} \text{ eV}$, and the second knee occurs at $10^{17.04} \text{ eV}$. We do not perform the unfolding analysis in this thesis, but instead use an easier, more straight-forward approach.

6.3.1 Light and heavy particles

To distinguish between the light and heavy particles, we plot the relation between the number of muons and the number of electrons detected by KASCADE corrected for the detector response bias, in Figure 6.4 for proton and iron simulations for three hadronic interaction models. As the dependencies behave similarly for all hadronic interaction models, we fit the relation between number of muons and electrons with a linear function for each of the two primaries. It should be noted that this approach is only relevant for $\log N_e^{\text{corr}} > 5$ for both reconstructions, due to the non-linear shape of the relation between the number of muons and electrons otherwise.

We then get the equations for pure proton showers

$$\log N_{\mu,p}^{\text{corr}} = (0.318 \pm 0.004) + (0.761 \pm 0.001) \cdot \log N_e^{\text{corr}} \quad (6.3)$$

and for pure iron showers

$$\log N_{\mu,Fe}^{\text{corr}} = (0.445 \pm 0.006) + (0.8032 \pm 0.0013) \cdot \log N_e^{\text{corr}}, \quad (6.4)$$

from which we derive the equation which divides the light particle region and heavy particle region

$$\log N_{\mu,\text{mid}}^{\text{corr}} = (0.382 \pm 0.004) + (0.7821 \pm 0.0008) \cdot \log N_e^{\text{corr}}, \quad (6.5)$$

meaning that for showers with

- $\log N_{\mu}^{\text{corr}} \geq \log N_{\mu,\text{mid}}^{\text{corr}}(\log N_e^{\text{corr}})$, the initiating particle is classified as heavy,
- $\log N_{\mu}^{\text{corr}} < \log N_{\mu,\text{mid}}^{\text{corr}}(\log N_e^{\text{corr}})$, the initiating particle is classified as light.

The heavy region should contain dominantly iron-like and CNO-group-like showers, the light region proton-like and helium-like showers.

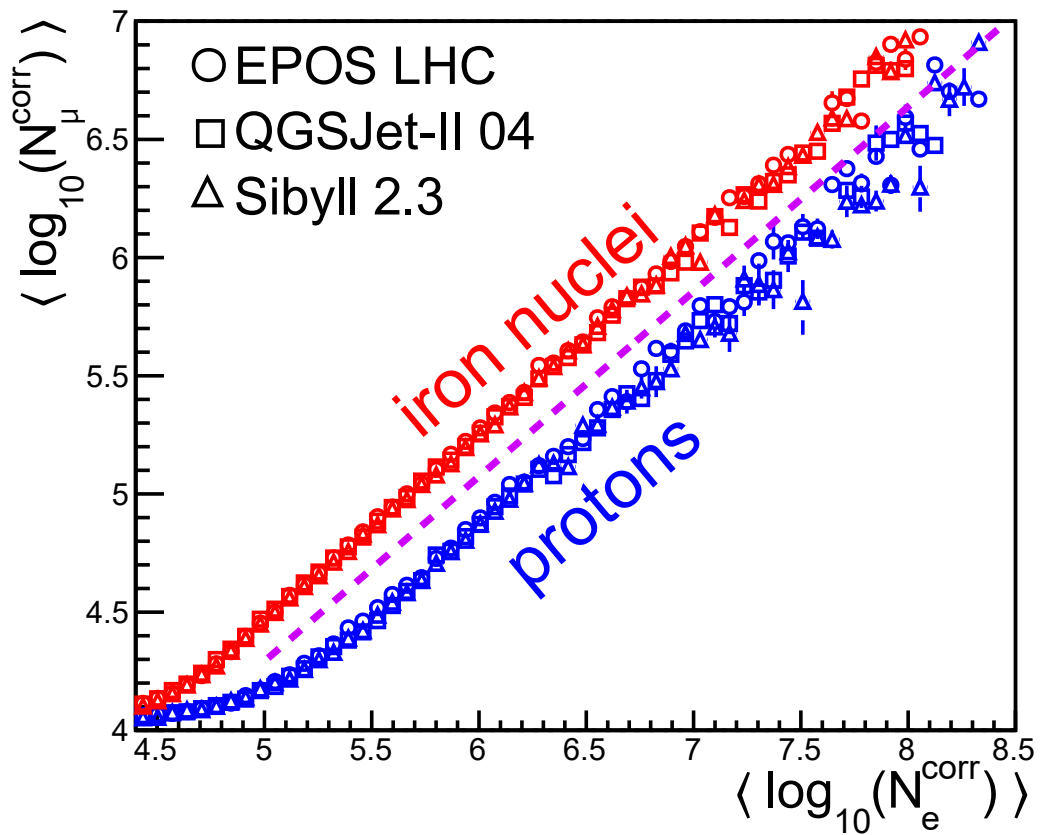


Figure 6.4: The relation between the mean reconstructed number of muons and the mean reconstructed number of electrons. The dashed purple line indicates the division between the light and heavy primaries, see Eq. 6.5.

We plot the resulting normalised energy spectra of light, heavy and all particles in Figure 6.5. The notable changes in the spectral index are indicated with correspondingly colored arrows. Note the re-scaling of flux by cube of energy.

It should be noted that the energy spectra are burdened by uncertainties mainly dominated by the inadequate categorising for light and heavy particles for energies

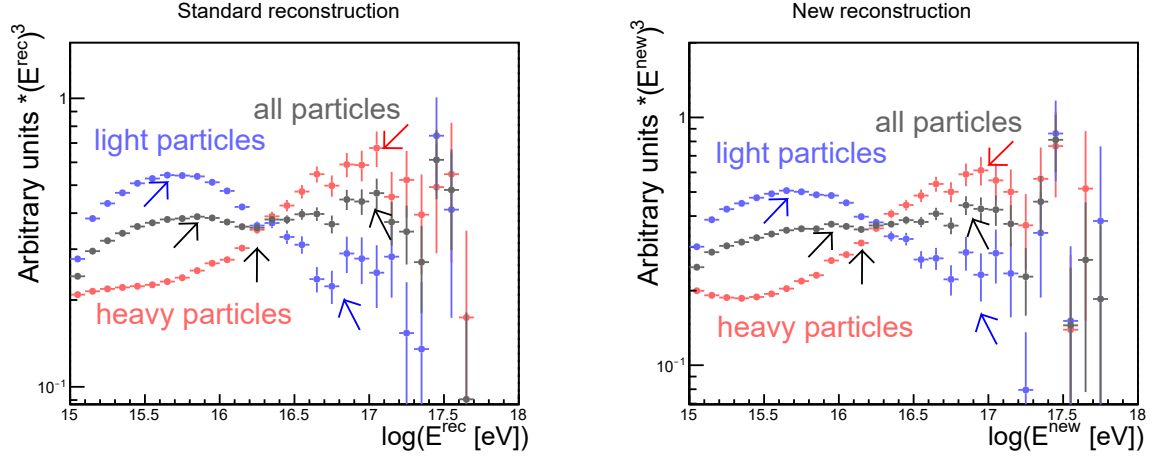


Figure 6.5: The normalised energy fluxes scaled by E^3 in arbitrary units of light particles (blue), heavy particles (red) and all particles (black) for the old energy reconstruction (**left**) and the new energy reconstruction (**right**).

below $\sim 10^{15.5}$ eV and low statistics for energies above $\sim 10^{17}$ eV. In both reconstructions, we see the shape of the total energy spectrum as detected by TALE: two broad maximums with centers with a dip between them. The centers of the broad maxima are at $E \sim 10^{15.85}$ eV and $E \sim 10^{17.05}$ eV for the old reconstruction, $E \sim 10^{15.95}$ eV and $E \sim 10^{16.85}$ eV for the new reconstruction. The dip can be clearly seen in the old reconstruction, but is less eminent in the new reconstruction.

The energy spectra for light particles show clear steepening for energies above $E \sim 10^{15.65}$ eV for both the old and new reconstruction, agreeing with the previous results. The energy spectra for heavy particles show a rising trend until the energy $\sim 10^{17}$ eV, where low statistics obscure the results. It should be noted that for energies above this low-statistics threshold, the heavy spectra decrease steeper than the light spectra. Another change for the heavy sample at the energy $\sim 10^{15.45}$ eV might be connected to the remaining part of the light particles due to imprecise selection.

6.3.2 Light, medium-heavy and heavy particles

We also observe the changes in the energy spectrum for light, heavy and medium-heavy particles. We take Eq. (6.3) and (6.4) into account, from which we derive the equations to divide the light, heavy and medium-heavy particle regions

$$\log N_{\mu, \text{Her}}^{\text{corr}} = (0.403 \pm 0.006) + (0.789 \pm 0.005) \cdot \log N_e^{\text{corr}}, \quad (6.6)$$

$$\log N_{\mu, \text{Ler}}^{\text{corr}} = (0.360 \pm 0.005) + (0.775 \pm 0.004) \cdot \log N_e^{\text{corr}}, \quad (6.7)$$

meaning that for showers with

- $\log N_{\mu}^{\text{corr}} > \log N_{\mu, \text{Her}}^{\text{corr}} (\log N_e^{\text{corr}})$, the initiating particle is classified as heavy,
- $\log N_{\mu, \text{Ler}}^{\text{corr}} (\log N_e^{\text{corr}}) < \log N_{\mu}^{\text{corr}} < \log N_{\mu, \text{Her}}^{\text{corr}} (\log N_e^{\text{corr}})$, the initiating particle is classified as medium-heavy,

- $\log N_\mu^{\text{corr}} < \log N_{\mu, \text{Ler}}^{\text{corr}}(\log N_e^{\text{corr}})$, the initiating particle is classified as light.

The heavy sample should contain dominantly iron-like showers, the light region should contain proton-like, and the medium-heavy showers should contain the CNO-group-like showers. The line separating between the light and medium-heavy particles approximately correlates with the relation between the number of muons and the number of electrons for helium and the line between medium-heavy and heavy particles of the CNO-group-like particles.

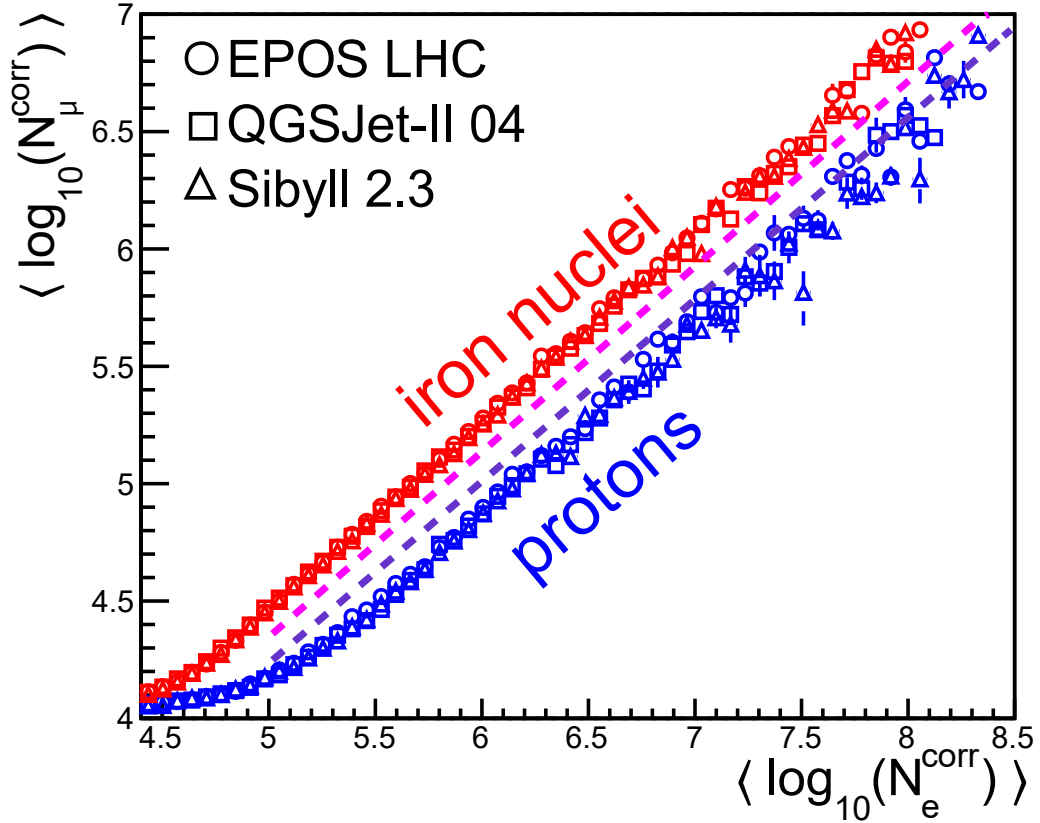


Figure 6.6: The relation between the mean reconstructed number of muons and the mean reconstructed number of electrons. The pink dashed line indicates the division between the heavy and medium-heavy primaries, see Eq. (6.6), and the purple dashed line indicates the division between the medium-heavy and light primaries, see Eq. (6.7).

Once again, these relations hold for $5 < \log N_e^{\text{corr}}$ for both reconstructions. We plot the resulting normalised spectra for light, heavy, medium-heavy and all particles in Figure 6.7 for both energy estimations. The notable changes in the spectral index are indicated with correspondingly colored arrows.

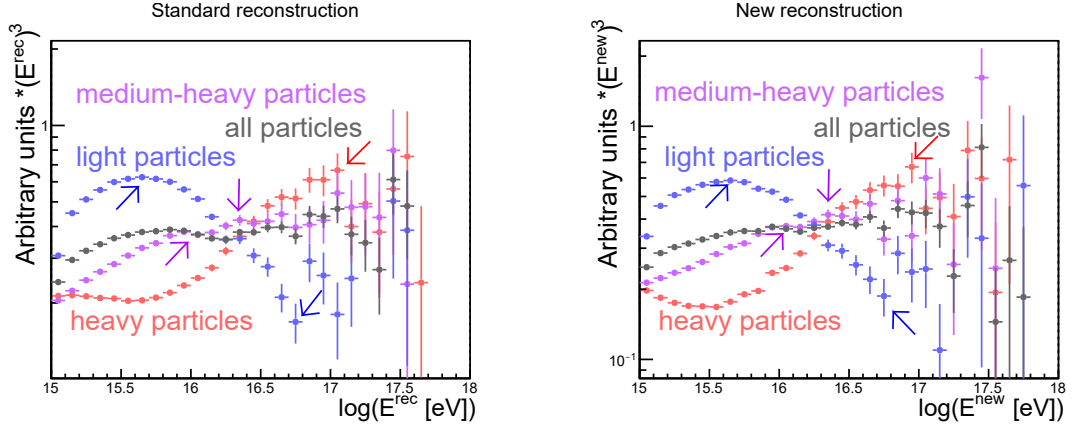


Figure 6.7: The normalised energy fluxes scaled by E^3 in arbitrary units of light particles (blue), medium-heavy particles (pink), heavy particles (red) and all particles (black).

The spectral index break positions remain the same for the light particles as in the previous case. The heavy and light spectra in Figure 6.5 appear flatter than in Figure 6.7, which may be caused by the contribution of the medium-heavy particles. The shape of the medium-heavy particles' spectra seems to mimic the shape of the full spectrum.

The features observed in this work are consistent with the breaks reported by the KASCADE-Grande collaboration in [31], see Figure 3.3, where more profound study using the unfolding method was applied.

Conclusions

In this work, basic information about cosmic rays, including the mass composition, energy spectrum and the evolution of extensive air showers were introduced. The experiment KASCADE and its cosmic ray data centre KCDC were introduced and described, along with the data and simulations used for our analysis.

The energy reconstruction formula currently used by KASCADE uses the number of muons, the number of electrons and the zenith angle measured at ground to estimate the energy of the primary cosmic ray. We show that the biases of the estimated shower energy can be decreased by introducing the lateral shape parameter, or age of the shower parameter, s^{rec} . Within a new approach to reconstruct the energy of the primary cosmic ray, we sum the calorimetric energy and the invisible energy not deposited in the atmosphere. Our data-driven method to obtain the invisible energy is based on an approach used by the Pierre Auger Observatory.

To derive the universal relation between the invisible energy and the number of muons measured at ground by KASCADE, we use additional showers that were generated with the same hadronic interaction models and primary types as those used in KCDC simulations containing the information about the longitudinal shower development.

The calibration of the calorimetric energy was applied on the KASCADE simulations provided by KCDC. We observe the dependence between the calorimetric energy and the number of charged particles transformed to the zero zenith angle and show the obtained parameters of this relation in relation with the reconstructed age parameter s^{rec} . We show the new reconstruction process in detail.

We compare the biases and resolution of shower energy estimated from KASCADE simulations provided by KCDC. The new formula decreases the bias differences between different primaries and provides better energy resolution, hinting at a possible improvement of the energy reconstruction method, seeing as the primary type is unknown upon detection. The new formula also produces biases more monotonous with respect to the primary energy, as opposed to the standard energy reconstruction, which shows dependence on the primary energy.

We estimate the consequences of this new energy reconstruction. We observe the change in the energy dependence of muon number. While some studies have shown an excess in the measured number of muons over expectations, we find that the current energy reconstruction does not seem to follow this trend, and instead shows that the KASCADE experiment detected slightly less muons than predicted. This

goes in line with recent study by the WHISP working group on the combined analysis of muon data at cosmic-ray energies above 1 PeV [37].

We have also investigated the invisible energy fraction that is relevant for optical measurements. The invisible energy fraction follows similar trend as the energy dependence of the muon number, as our analysis derives the invisible energy directly from the number of muons. The invisible energy fraction is smaller than in recent studies [44].

We derive a relation between the detected number of muons and the detected number of electrons for both the standard and the new reconstruction methods to differentiate between light and heavy particles, and between light, heavy and medium-heavy particles. When differentiating between light and heavy particles, the resulting spectra appear flatter than when differentiating between light, medium-heavy and heavy particles. The heavy particles spectrum shows a rising trend until the energy 10^{17} eV, where low statistics obscure the results. In both methods of differentiation and in both standard and new reconstruction methods, we see a clear steepening in the light energy spectrum at $E \sim 10^{15.65}$ eV, indicating another spectral feature for medium-heavy and heavy particles at higher energies proportional approximately to the particles' charges. These results go in line with the KASCADE-Grande results [31].

The presented results were not studied for systematic uncertainties, such as the systematic uncertainties in the measurements of muons and electrons, the hadronic interaction models and their differences, the uncertainties in the mass composition, or the systematic uncertainty of the energy estimation method. We further propose an improvement of our results, namely by performing the unfolding analysis to distinguish between different masses of particles, using a larger data sample, such as not only using additional data recorded by the experiment KASCADE, but also implementing data recorded by the KASCADE-Grande extension, or using an improved hadronic interaction model Sibyll 2.3d.

Bibliography

- [1] A. De Angelis and M. J. M. Pimenta. *Introduction to Particle and Astroparticle Physics: Questions to the Universe*. Springer, 2015.
- [2] K.-H. Kampert and M. Unger. Measurements of the Cosmic Ray Composition with Air Shower Experiments. *Astroparticle Physics*, 35:660 – 678, 2012. URL <https://10.1016/j.astropartphys.2012.02.004>.
- [3] T. Abu-Zayyad et al. The Knee and the Second Knee of the Cosmic-Ray Energy Spectrum, 2018. URL <https://arxiv.org/abs/1803.07052>.
- [4] P. Abreu et al. The ultra-high-energy cosmic-ray sky above 32 EeV viewed from the Pierre Auger Observatory. *PoS, ICRC2021:307*, 2021. URL <https://10.22323/1.395.0307>.
- [5] D. J. Bird et al. Detection of a cosmic ray with measured energy well beyond the expected spectral cutoff due to cosmic microwave radiation. *The Astrophysical Journal*, 441:144, Mar 1995. doi: 10.1086/175344. URL <https://doi.org/10.1086%2F175344>.
- [6] T. Antoni et al. The cosmic-ray experiment KASCADE. *Nuclear Instruments and Methods in Physics Research Section A: Accelerators, Spectrometers, Detectors and Associated Equipment*, 513(3):490–510, 2003. ISSN 0168-9002. doi: [https://doi.org/10.1016/S0168-9002\(03\)02076-X](https://doi.org/10.1016/S0168-9002(03)02076-X). URL <https://www.sciencedirect.com/science/article/pii/S016890020302076X>.
- [7] A. Haungs et al. The KASCADE Cosmic-ray Data Centre KCDC: granting open access to astroparticle physics research data. *The European Physical Journal C*, 78(9), Sep 2018. ISSN 1434-6052. doi: 10.1140/epjc/s10052-018-6221-2. URL <http://dx.doi.org/10.1140/epjc/s10052-018-6221-2>.
- [8] D. Perkins. *Particle Astrophysics: Second Edition*. Oxford University Press, 2009.
- [9] M. S. Longair. *High Energy Astrophysics: Third Edition*. Cambridge University Press, 2011.
- [10] K. Greisen. End to the Cosmic-Ray Spectrum? *Phys. Rev. Lett.*, 16:748–750, Apr 1966. doi: 10.1103/PhysRevLett.16.748. URL <https://link.aps.org/doi/10.1103/PhysRevLett.16.748>.

- [11] G.T. Zatsepin and V.A. Kuzmin. Upper limit of the spectrum of cosmic rays. *JETP Lett.*, 4:78–80, 1966.
- [12] H. Dembinski et al. Data-driven model of the cosmic-ray flux and mass composition from 10 GeV to 10^{11} GeV, 2017.
- [13] A. López-Oramas. Multi-year Campaign of the Gamma-Ray Binary LS I +61° 303 and Search for VHE Emission from Gamma-Ray Binary Candidates with the MAGIC Telescopes. Apr 2015. URL <https://10.13140/RG.2.1.4140.4969>.
- [14] T. Matthews. A Heitler model of extensive air showers. *Astroparticle Physics*, 22:387 – 397, 2005. URL <https://10.1016/j.astropartphys.2004.09.003>.
- [15] W. Heitler. *The quantum theory of radiation*. Courier Corporation, 1984.
- [16] T. Bergmann et al. One-dimensional Hybrid Approach to Extensive Air Shower Simulation. *Astroparticle Physics*, 26:420 – 432, 2007. URL <https://10.1016/j.astropartphys.2006.08.005>.
- [17] D. Heck and J. Knapp. Upgrade of the Monte Carlo code CORSIKA to simulate extensive air showers with energies $> 10^{20}$ eV. 1998. URL <http://bibliothek.fzk.de/zb/berichte/FZKA6097.pdf>.
- [18] W. R. Nelson, H. Hirayama, and D. W. O. Rogers. EGS4 code system. Dec 1985. URL <https://www.osti.gov/biblio/6137659>.
- [19] A. B. Migdal. Bremsstrahlung and Pair Production in Condensed Media at High Energies. *Phys. Rev.*, 103:1811–1820, Sep 1956. doi: 10.1103/PhysRev.103.1811. URL <https://link.aps.org/doi/10.1103/PhysRev.103.1811>.
- [20] R. M. Sternheimer, S. M. Seltzer, and M. J. Berger. Density effect for the ionization loss of charged particles in various substances. *Phys. Rev. B*, 26: 6067–6076, Dec 1982. doi: 10.1103/PhysRevB.26.6067. URL <https://link.aps.org/doi/10.1103/PhysRevB.26.6067>.
- [21] A. Fasso’ et al. The physics models of FLUKA: status and recent development, 2003.
- [22] R. Engel et al. The hadronic interaction model Sibyll – past, present and future. *EPJ Web of Conferences*, 145:08001, 2017. URL <https://10.1051/epjconf/201614508001>.
- [23] R. Engel et al. Hadronic interaction model sibyll 2.3d and extensive air showers. *Physical Review D*, 102(6), 9 2020. ISSN 2470-0010. doi: 10.1103/PhysRevD.102.063002. URL <https://www.osti.gov/biblio/1659547>.
- [24] S. Ostapchenko and D. Heck. Hadronic Interactions in QGSJET-II: Physics and Results. 2005.

- [25] S. Ostapchenko. Monte Carlo treatment of hadronic interactions in enhanced Pomeron scheme: QGSJET-II model. *Physical Review D*, 83(1), Jan 2011. ISSN 1550-2368. doi: 10.1103/physrevd.83.014018. URL <http://dx.doi.org/10.1103/PhysRevD.83.014018>.
- [26] T. Pierog and K. Werner. EPOS Model and Ultra High Energy Cosmic Rays. *Nuclear Physics B - Proceedings Supplements*, 196:102–105, Dec 2009. ISSN 0920-5632. doi: 10.1016/j.nuclphysbps.2009.09.017. URL <http://dx.doi.org/10.1016/j.nuclphysbps.2009.09.017>.
- [27] T. Pierog et al. EPOS LHC: Test of collective hadronization with data measured at the CERN Large Hadron Collider. *Physical Review C*, 92(3), Sep 2015. ISSN 1089-490X. doi: 10.1103/physrevc.92.034906. URL <http://dx.doi.org/10.1103/PhysRevC.92.034906>.
- [28] J. Wochele et al. KCDC User Manual, 2022. URL https://kcdc.iap.kit.edu/static/pdf/kcdc_mainpage/kcdc-Manual.pdf.
- [29] T. Antoni et al. KASCADE measurements of energy spectra for elemental groups of cosmic rays: Results and open problems. *Astroparticle Physics*, 24(1–2):1–25, Sep 2005. ISSN 0927-6505. doi: 10.1016/j.astropartphys.2005.04.001. URL <http://dx.doi.org/10.1016/j.astropartphys.2005.04.001>.
- [30] W. D. Apel et al. Kneelike Structure in the Spectrum of the Heavy Component of Cosmic Rays Observed with KASCADE-Grande. *Physical Review Letters*, 107(17), Oct 2011. ISSN 1079-7114. doi: 10.1103/physrevlett.107.171104. URL <http://dx.doi.org/10.1103/PhysRevLett.107.171104>.
- [31] W.D. Apel et al. KASCADE-Grande measurements of energy spectra for elemental groups of cosmic rays. *Astroparticle Physics*, 47:54–66, Jul 2013. ISSN 0927-6505. doi: 10.1016/j.astropartphys.2013.06.004. URL <http://dx.doi.org/10.1016/j.astropartphys.2013.06.004>.
- [32] S. Schoo et al. Latest Results of KASCADE-Grande. page 545, 08 2017. URL <https://10.22323/1.301.0545>.
- [33] J. Wochele et al. KCDC Simulation Manual - KASCADE, GRANDE and CALORIMETER Simulations, 2022. URL https://kcdc.iap.kit.edu/static/pdf/kcdc_mainpage/kcdc-Simulation-Manual.pdf.
- [34] J. Vicha et al. Invisible Energy from KASCADE Data. In *Proceedings of 36th International Cosmic Ray Conference — PoS(ICRC2019)*, volume 358, page 453, 2019. URL <https://10.22323/1.358.0453>.
- [35] V. Novotny et al. Energy spectrum of cosmic rays measured using the Pierre Auger Observatory. In *Proceedings of 37th International Cosmic Ray Conference — PoS(ICRC2021)*, volume 395, page 324, 2021. URL <https://10.22323/1.395.0324>.

- [36] A. Aab et al. Data-driven estimation of the invisible energy of cosmic ray showers with the Pierre Auger Observatory. *Physical Review D*, 100(8), Oct 2019. ISSN 2470-0029. doi: 10.1103/physrevd.100.082003. URL <http://dx.doi.org/10.1103/PhysRevD.100.082003>.
- [37] J.C. Arteaga Velazquez. A report by the WHISP working group on the combined analysis of muon data at cosmic-ray energies above 1 PeV. In *Proceedings of 38th International Cosmic Ray Conference — PoS(ICRC2023)*, volume 444, page 446, 2023. URL <https://10.22323/1.444.0466>.
- [38] W.D. Apel et al. Probing the evolution of the EAS muon content in the atmosphere with KASCADE-Grande. *Astroparticle Physics*, 95:25–43, Oct 2017. doi: 10.1016/j.astropartphys.2017.07.001. URL <https://doi.org/10.1016%2Fj.astropartphys.2017.07.001>.
- [39] A. Ivanov, M. I. Pravdin, and A. Saburov. Modelling a relation between shower age and lateral distribution parameters of extensive air showers of cosmic rays. *International Journal of Modern Physics D*, 20, May 2012. URL <https://10.1142/S0218271811019463>.
- [40] K Greisen. Cosmic Ray Showers. *Annual Review of Nuclear Science*, 10(1): 63–108, 1960. doi: 10.1146/annurev.ns.10.120160.000431. URL <https://doi.org/10.1146/annurev.ns.10.120160.000431>.
- [41] J. Velazquez. Estimations of the muon content of cosmic ray air showers between 10 PeV and 1 EeV from KASCADE-Grande data. page 376, Jul 2021. URL <https://10.22323/1.395.0376>.
- [42] L. Cazon. Working Group Report on the Combined Analysis of Muon Density Measurements from Eight Air Shower Experiments, 2020.
- [43] V. Novotný. Measurement of the spectrum of cosmic rays above $10^{16.5}$ eV with Cherenkov-dominated events at the Pierre Auger Observatory. In *Proceedings of 36th International Cosmic Ray Conference — PoS(ICRC2019)*, volume 358, page 374, 2019. URL <https://10.22323/1.358.0374>.
- [44] Jakub Vicha, Vladimír Novotný, and Jan Ebr. Data-driven Estimation of Invisible Energy below EeV. In *Proceedings of 38th International Cosmic Ray Conference — PoS(ICRC2023)*, volume 444, page 497, 2023. URL <https://10.22323/1.444.0497>.
- [45] G. Kulikov and G. Khristiansen. On the Size Spectrum of Extensive Air Showers. *Sov. Phys.*, 1959.
- [46] B. Peters. Primary cosmic radiation and extensive air showers. *Nuovo Cim.*, 22(4):800–819, 1961. URL <https://10.1007/bf02783106>.

Appendix A

Energy reconstruction

A.1 Values of the new energy reconstruction

θ^{rec}	$0^\circ\text{-}12.31^\circ$	$12.31^\circ\text{-}17.41^\circ$	$17.41^\circ\text{-}21.5^\circ$	$21.5^\circ\text{-}25^\circ$
p_0^e	6.7 ± 0.5	6.5 ± 0.6	4.7 ± 0.6	4.9 ± 0.6
p_1^e	-2.8 ± 0.3	-2.7 ± 0.4	-1.5 ± 0.4	-1.7 ± 0.4
p_2^e	0.36 ± 0.08	0.35 ± 0.11	0.10 ± 0.05	0.10 ± 0.09
p_3^e	-0.007 ± 0.006	-0.007 ± 0.005	0.026 ± 0.011	0.021 ± 0.011
p_4^e	-0.0009 ± 0.0004	-0.0008 ± 0.0004	-0.0022 ± 0.0004	-0.0019 ± 0.0005
p_0^μ	-36.4 ± 1.8	-36.9 ± 1.8	-38.8 ± 1.9	-48 ± 2
p_1^μ	31.2 ± 1.4	31.5 ± 1.4	32.7 ± 1.5	39.9 ± 1.6
p_2^μ	-9.9 ± 0.4	-9.9 ± 0.4	-10.2 ± 0.4	-12.3 ± 0.5
p_3^μ	1.36 ± 0.05	1.36 ± 0.05	1.39 ± 0.06	1.66 ± 0.06
p_4^μ	-0.070 ± 0.003	-0.069 ± 0.002	-0.070 ± 0.003	-0.083 ± 0.003

Table A.1: Parameters of Eq. (5.4) to correct for the detector response to the number of electrons p_i^e and muons p_i^μ along with the appropriate zenith angle bin.

$$\begin{aligned}
 \log E_{\text{Inv}} &= \log C(\cos \theta^{\text{rec}}) + \log N_\mu^{\text{corr}} \cdot \delta(\cos \theta^{\text{rec}}), \\
 \log C &= (11.14 \pm 0.08) - (0.8 \pm 0.2) \cdot \cos \theta^{\text{rec}} + (0.17 \pm 0.13) \cdot \cos^2 \theta^{\text{rec}}, \\
 \delta &= (0.935 \pm 0.017) - (0.04 \pm 0.03) \cdot \cos \theta^{\text{rec}} + (0.4 \pm 0.3) \cdot \cos^2 \theta^{\text{rec}}.
 \end{aligned} \tag{A.1}$$

$$\begin{aligned}
 N_{\text{ch}}(0^\circ) &= N_\mu^{\text{corr}}(0^\circ) + N_e^{\text{corr}}(0^\circ), \\
 \log N_\mu^{\text{corr}}(0^\circ) &= \log N_\mu^{\text{corr}} - (0.0008 \pm 0.0007) \cdot \theta^{\text{rec}} \\
 &\quad + (0.000119 \pm 0.000019) \cdot \theta^{\text{rec}^2}, \\
 \log N_e^{\text{corr}}(0^\circ) &= \log N_e^{\text{corr}} - (0.005 \pm 0.001) \cdot \theta^{\text{rec}} \\
 &\quad + (0.00064 \pm 0.00002) \cdot \theta^{\text{rec}^2}.
 \end{aligned} \tag{A.2}$$

$$\begin{aligned}
\log E_{\text{Cal}} &= \log D(s^{\text{rec}}) + \log N_{\text{ch}}(0^\circ) \cdot \omega(s^{\text{rec}}), \\
\log D &= (67 \pm 3) - (239 \pm 16) \cdot s^{\text{rec}} + (360 \pm 20) \cdot s^{\text{rec}^2} \\
&\quad - (235 \pm 17) \cdot s^{\text{rec}^3} + (56 \pm 4) \cdot s^{\text{rec}^4}, \\
\omega &= -(6.8 \pm 0.7) + (31 \pm 3) \cdot s^{\text{rec}} - (45 \pm 5) \cdot s^{\text{rec}^2} \\
&\quad + (28 \pm 3) \cdot s^{\text{rec}^3} - (6.7 \pm 0.8) \cdot s^{\text{rec}^4}.
\end{aligned} \tag{A.3}$$

$$\begin{aligned}
E_{\text{Cal}}^{\text{corr}} &= \frac{E_{\text{Cal}}}{p_5(\log E_{\text{Cal}}) + 1}, \\
p_5(\log E_{\text{Cal}}) &= -(3100 \pm 600) + (750 \pm 180) \cdot \log E_{\text{Cal}} \\
&\quad - (70 \pm 20) \cdot \log^2 E_{\text{Cal}} + (3.1 \pm 1.4) \cdot \log^3 E_{\text{Cal}} \\
&\quad - (0.06 \pm 0.04) \cdot \log^4 E_{\text{Cal}} \\
&\quad + (0.0003 \pm 0.0002) \cdot \log^5 E_{\text{Cal}}.
\end{aligned} \tag{A.4}$$

A.2 Biases and resolutions of other models

A.2.1 Biases with respect to true energy

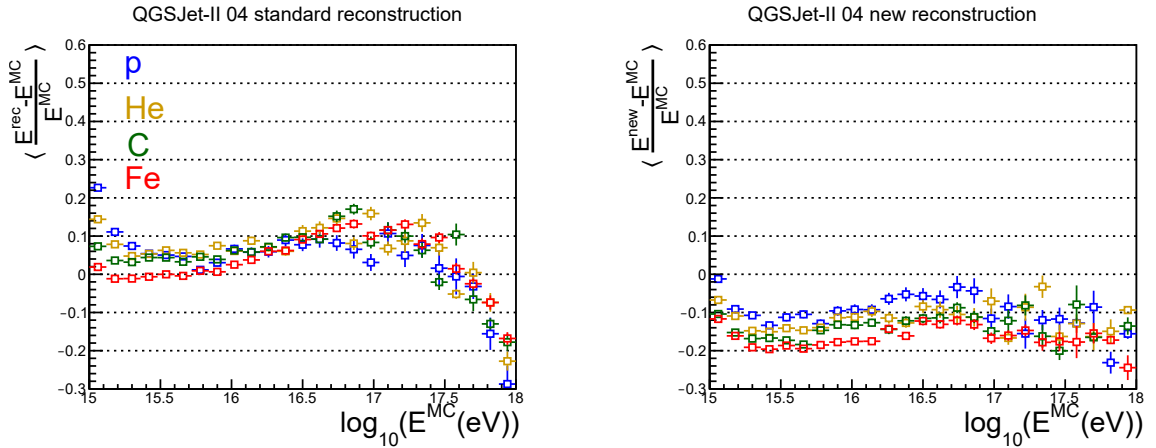


Figure A.1: The energy evolutions of average relative differences between the reconstructed and true shower energies for the hadronic interaction model QGSJet-II 04 estimated using the KASCADE formula (**left**) and using the new energy formula (**right**), see Eq. (5.4) to (5.9) in Section 5.3.

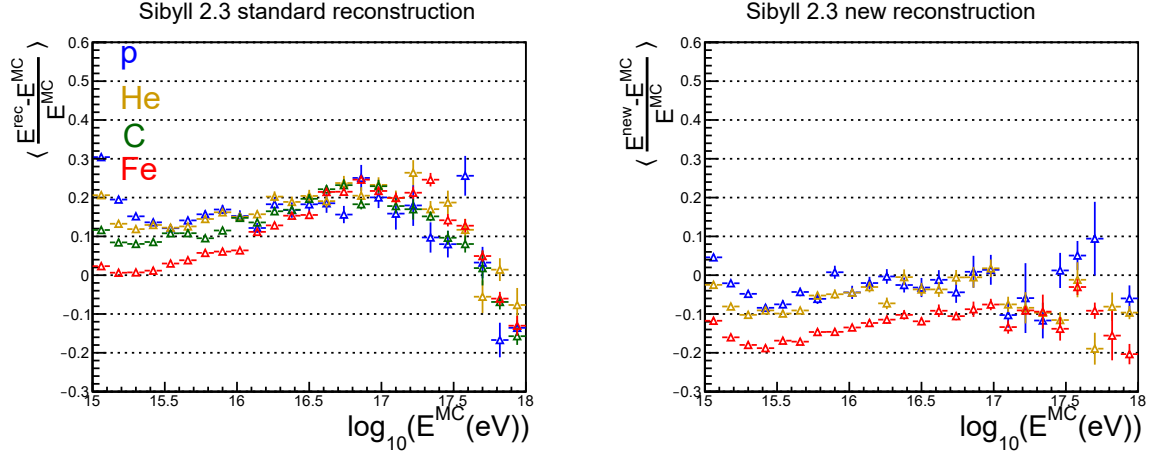


Figure A.2: The energy evolutions of average relative differences between the reconstructed and true shower energies for the hadronic interaction model Sibyll 2.3 estimated using the KASCADE formula (**left**) and using the new energy formula (**right**), see Eq. (5.4) to (5.9) in Section 5.3.

A.2.2 Resolutions with respect to true energy

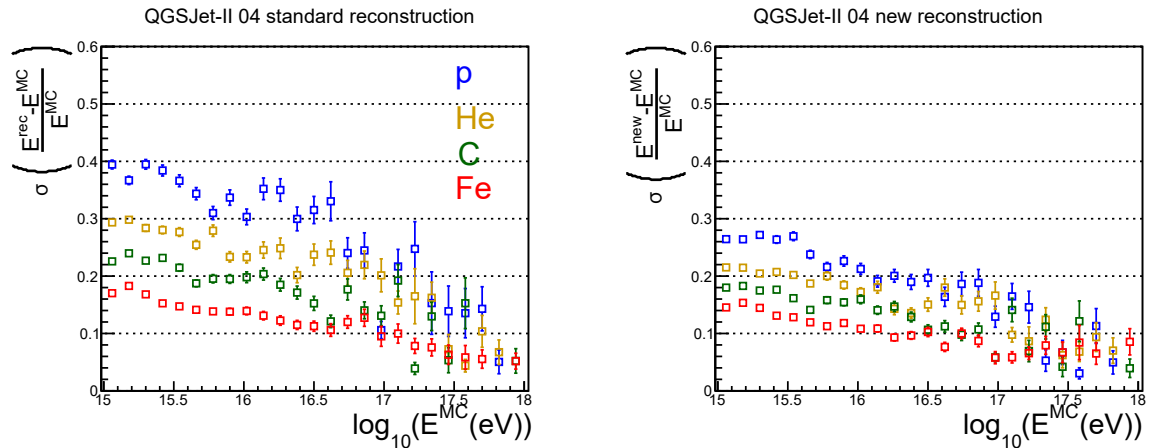


Figure A.3: The energy evolutions of the standard deviation of relative differences between reconstructed and true shower energies for the hadronic interaction model QGSJet-II 04 estimated using the KASCADE formula (**left**) and using the new energy formula (**right**). Bins with less than 3 events are not included.

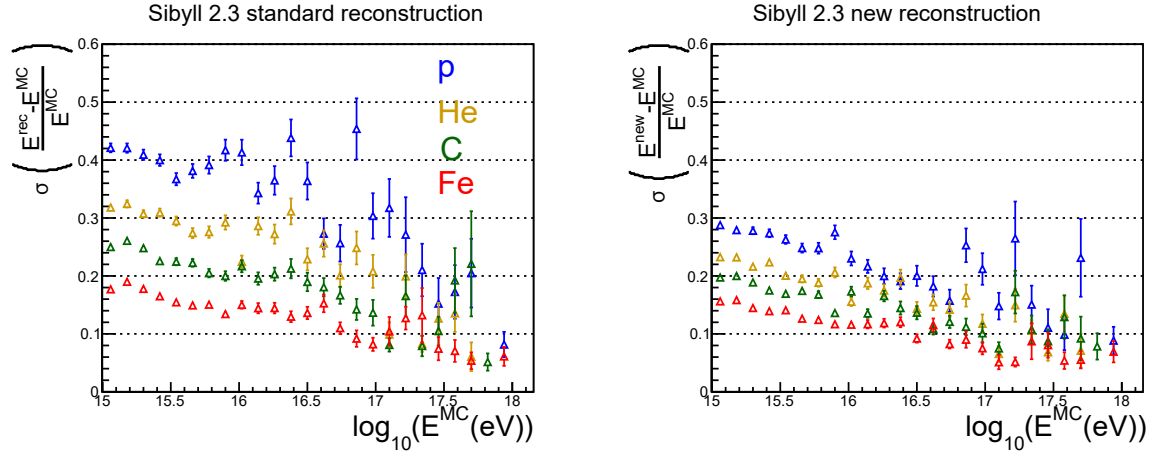


Figure A.4: The energy evolutions of the standard deviation of relative differences between reconstructed and true shower energies for the hadronic interaction model Sibyll 2.3 estimated using the KASCADE formula (**left**) and using the new energy formula (**right**). Bins with less than 3 events are not included.

A.2.3 Biases with respect to reconstructed energy

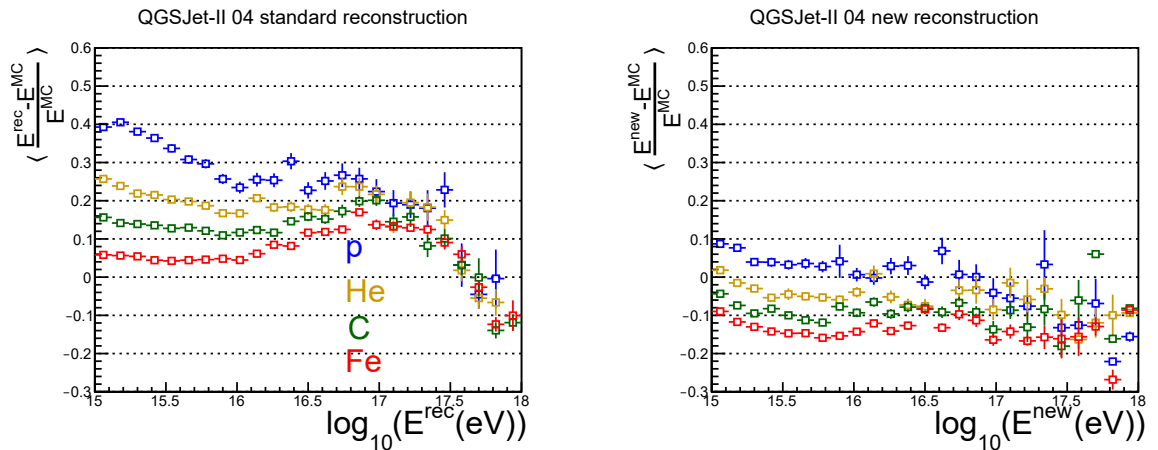


Figure A.5: The energy evolutions of average relative differences between the reconstructed and true shower energies for the hadronic interaction model QGSJet-II 04 dependent on reconstructed energies estimated using the KASCADE formula (**left**) and using the new energy formula (**right**), see Eq. (5.4) to (5.9) in Section 5.3.

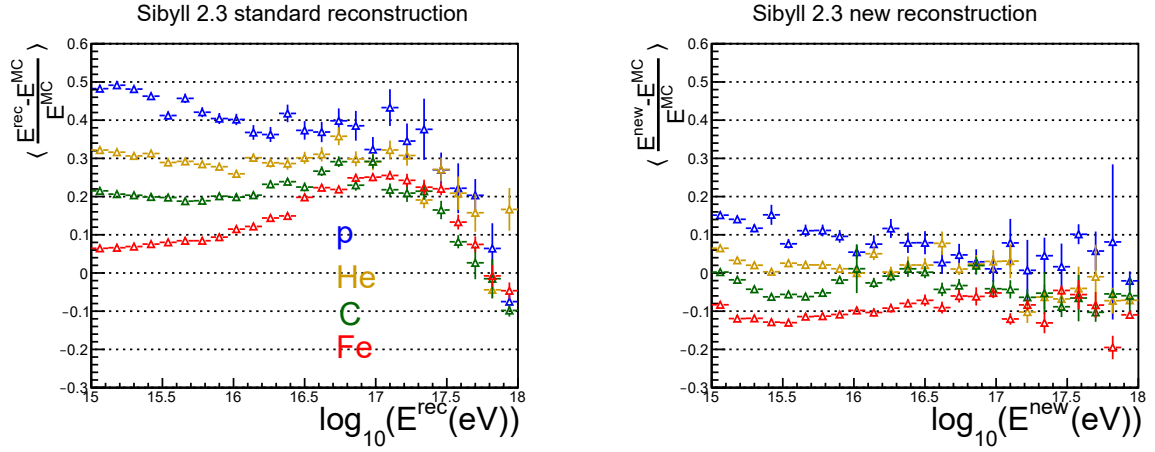


Figure A.6: The energy evolutions of average relative differences between the reconstructed and true shower energies for the hadronic interaction model Sibyll 2.3 dependent on reconstructed energies estimated using the KASCADE formula (**left**) and using the new energy formula (**right**), see Eq. (5.4) to (5.9) in Section 5.3.